Molecular Cell

Article

Nuclear pore permeability and fluid flow are modulated by its dilation state

Graphical abstract

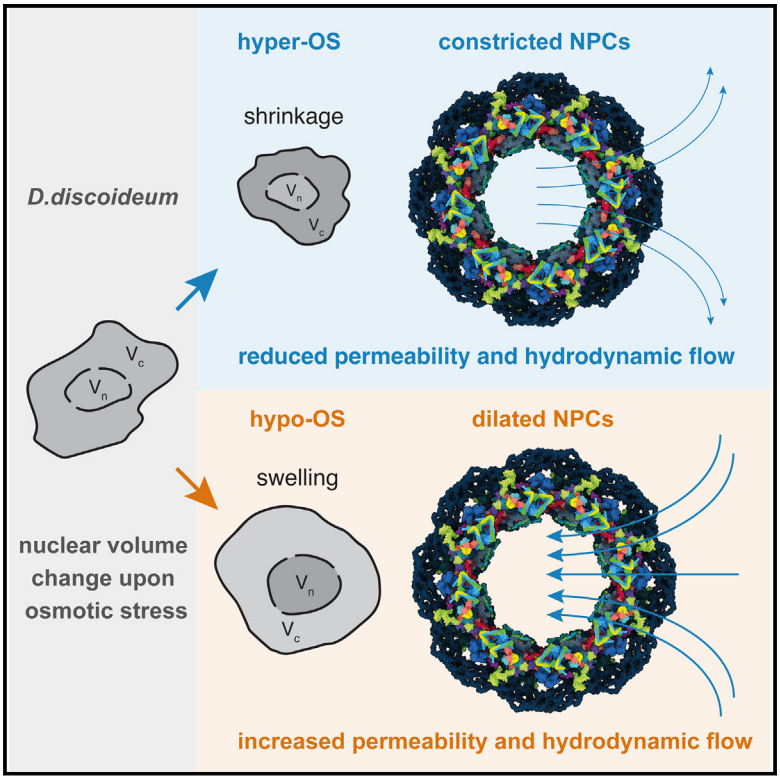

Authors

Patrick C. Hoffmann, Hyuntae Kim, Agnieszka Obarska-Kosinska, ..., Beata Turoňová, Gerhard Hummer, Martin Beck

Correspondence

gerhard.hummer@biophys.mpg.de (G.H.), martin.beck@biophys.mpg.de (M.B.)

In brief

Hoffmann et al. describe within cells how the *Dictyostelium discoideum* nuclear pore complex structure constricts and dilates as a consequence of osmotic stress. Based on their experimental findings, they propose a hydrodynamics model and quantify fluid flow across nuclear pore complexes under conditions when nuclei change their volume rapidly.

Highlights

- *D. discoideum* NPCs have a unique scaffold architecture
- Fast volume change during osmotic stress creates directional fluid flow through NPCs
- NPC diameter and effective opening change rapidly upon osmotic stress
- Fluid flow through NPCs can be conceptualized by hydrodynamics as porous flow

Hoffmann et al., 2025, Molecular Cell *85*, 537–554
February 6, 2025
https://doi.org/10.1016/j.molcel.2024.11.038

CellPress

Molecular Cell

CellPress
OPEN ACCESS

Article

Nuclear pore permeability and fluid flow are modulated by its dilation state

Patrick C. Hoffmann,[1,9] Hyuntae Kim,[2,3,9] Agnieszka Obarska-Kosinska,[1,9] Jan Philipp Kreysing,[1,3] Eli Andino-Frydman,[1] Sergio Cruz-León,[2] Erica Margiotta,[1] Lenka Cernikova,[4,5] Jan Kosinski,[4,5,6] Beata Turoňová,[1] Gerhard Hummer,[2,7,*] and Martin Beck[1,8,10,*]

[1]Department of Molecular Sociology, Max Planck Institute of Biophysics, Max-von-Laue-Straße 3, 60438 Frankfurt am Main, Germany
[2]Department of Theoretical Biophysics, Max Planck Institute of Biophysics, Max-von-Laue-Straße 3, 60438 Frankfurt am Main, Germany
[3]IMPRS on Cellular Biophysics, Max-von-Laue-Straße 3, 60438 Frankfurt am Main, Germany
[4]European Molecular Biology Laboratory Hamburg, 22607 Hamburg, Germany
[5]Centre for Structural Systems Biology (CSSB), Notkestraße 85, 22607 Hamburg, Germany
[6]Structural and Computational Biology Unit, European Molecular Biology Laboratory, Meyerhofstraße 1, 69117 Heidelberg, Germany
[7]Institute of Biophysics, Goethe University Frankfurt, 60438 Frankfurt am Main, Germany
[8]Institute of Biochemistry, Goethe University Frankfurt, 60438 Frankfurt am Main, Germany
[9]These authors contributed equally
[10]Lead contact
*Correspondence: gerhard.hummer@biophys.mpg.de (G.H.), martin.beck@biophys.mpg.de (M.B.)
https://doi.org/10.1016/j.molcel.2024.11.038

SUMMARY

Changing environmental conditions necessitate rapid adaptation of cytoplasmic and nuclear volumes. We use the slime mold *Dictyostelium discoideum*, known for its ability to tolerate extreme changes in osmolarity, to assess which role nuclear pore complexes (NPCs) play in achieving nuclear volume adaptation and relieving mechanical stress. We capitalize on the unique properties of *D. discoideum* to quantify fluid flow across NPCs. *D. discoideum* has an elaborate NPC structure *in situ*. Its dilation state affects NPC permeability for nucleocytosolic flow. Based on mathematical concepts adapted from hydrodynamics, we conceptualize this phenomenon as porous flow across NPCs, which is distinct from canonically characterized modes of nucleocytoplasmic transport because of its dependence on pressure. Viral NPC blockage decreased nucleocytosolic flow. Our results may be relevant for any biological conditions that entail rapid nuclear size adaptation, including metastasizing cancer cells, migrating cells, or differentiating tissues.

INTRODUCTION

Nuclear pore complexes (NPCs) are large membrane protein complexes embedded in the nuclear membranes and consist of over 1,000 copies of ~30 individual nucleoporin proteins (Nups) (reviewed by Knockenhauer and Schwartz,[1] Hampoelz et al.,[2] Lin and Hoel,[3] and Beck and Hurt[4]). The central channel of the NPC functions as a permeability barrier between cyto- and nucleoplasm and facilitates two well-characterized types of nucleocytoplasmic exchange: active transport supported by transport receptors and passive diffusion.[5–7] The FG-repeat-containing Nups (FG-Nups) within the central channel constitute a permeability barrier that allows the passive diffusion of small molecules, while limiting the passage of macromolecules larger than ~35 kDa.[8–10] Cargos above the barrier threshold rely on nuclear transport receptors for active transport through the central channel. Recent studies suggest that dynamic fluctuations of FG-repeats in the central channel may transiently alter the permeability barrier;[11,12] however, the exact organization of FG-Nups still remains subject to investigation.[5,12] The passive diffusion limit of cargo suggests a radius of around 2.6 nm for the FG-Nup barrier.[8]

For several species, including humans and yeast, the architecture of the structured NPC scaffold and its components have been studied extensively by X-ray crystallography, cryoelectron tomography (cryo-ET), and integrative modeling.[2,3] Meanwhile, an almost complete picture of these systems has been obtained.[13–17] It exhibits an 8-fold rotational symmetry and can be subdivided into three major parts: the cytosolic ring (CR), the inner ring (IR), and the nuclear ring (NR).[18] NPCs are composed of different subcomplexes, of which the Y-complex[19,20] is a prominent and structurally well-characterized constituent. Y-complexes form head-to-tail arranged rings, which are components of both NR and CR.[18] The eight spokes of the IR are anchored in the NE membrane and provide a binding platform for central channel FG-Nups.[21–23] At last, Nup210 forms a ring-shaped domain in the nuclear envelope (NE) lumen.[24,25]

In contrast to previous structural studies of NPCs on isolated nuclei, where NPCs are present in a conformationally constricted state, recent studies demonstrated that NPCs in cells are

conformationally dynamic and reside in a so-called dilated state.[26–29] In response to cues, such as energy depletion or hyperosmotic stress (hyper-OS), NPCs constrict into a conformational ground state.[26] Nuclear membrane tension has been proposed as a factor for NPC diameter adaptation,[26] where mechanical forces increase nuclear membrane tension and stretch the NPC scaffold leading to NPC dilation.[26] Besides potential alterations to nucleocytoplasmic transport,[26,30] the functional relevance of NPC diameter regulation remains understudied.

We use *Dictyostelium discoideum*, a soil-dwelling amoeba that evolved to tolerate drastic alterations in environmental conditions, to understand the functional relationship between the NPC and cellular adaptation to environmental changes, such as osmotic conditions. Slime molds require water films for survival at different stages of their life cycle and development.[31,32] Thus, they have successfully established means to endure fluctuations in humidity and solute availability. Understanding the mechanisms underlying such biological adaptation processes may become crucial in devising strategies to cope with ongoing global environmental changes. Generally, cells without the additional support of a cell wall react to osmotic gradients with swelling or shrinkage through influx or efflux of water. In response, cells stabilize and regulate their volume by transporting ions and organic osmolytes across their membranes.[33,34] In addition, some protists including *D. discoideum* have a specialized organelle, the contractile vacuole, which helps to maintain cellular osmotic homeostasis and to cope with conditions of extreme osmolarity. In hypotonic environments, the vacuole removes water from the cytosol and is periodically expelled from the cell when fluid-filled.[35,36] *D. discoideum* is known to adjust its cellular volume upon osmotic changes on remarkable spatiotemporal scales, which coincide with alterations to cytoskeleton and activation of signaling pathways.[37–41]

Volume changes in an organism directly affect the concentration of all intracellular constituents, including macromolecules.[42] Hyper-OS is known to promote molecular crowding, influencing the diffusion of molecules, viscosity, and molecular condensation.[43,44] Organelles, such as the nucleus, also respond to the altered environment by adjusting their volume accordingly. Under normal conditions, nuclear size is coupled to cell size.[45] The initial hypothesis that nuclear size is mainly linked to DNA content and chromatin compaction has been extended. Recent studies reported and modeled how the balance of colloid osmotic pressure of macromolecules localized in the two compartments regulates the nuclear-to-cell volume ratio.[46,47] Both studies describe osmotic pressure as the determining factor for the volume ratio, which can only be altered by changes to nuclear transport or expression.[46,47] The nuclear membrane is covered with NPCs and, as such, displays different membrane properties than other organellar membranes.[48,49] Acute alterations in cell volume and macromolecular concentration, which affect nuclear shape and volume, induce compensational fluid flow through NPCs and across the NE membrane to maintain the volume ratio. The magnitude of flow across the central channel of the NPC and its effects on nuclear homeostasis are currently unclear. Clarifying how NPCs influence and potentially modulate the nuclear size response, while at the same time maintaining nuclear integrity, is crucial for understanding how cells cope with extreme environmental changes.

Here, we present the *in situ* structure of the *D. discoideum* NPC scaffold and its changes upon osmotic stress. We capitalize on the unique properties of *D. discoideum* cells in their vegetative, unicellular state to quantify fluid flow across NPCs that results from changes in nuclear size. We propose that this phenomenon is best conceptualized using hydrodynamic principles as porous flow.

RESULTS

Cellular and nuclear volume adaptations occur within seconds to minutes in response to OS

In eukaryotes, nuclear and cell size are coupled under normal growth conditions.[45] Although osmotic stress has immediate and drastic effects on the overall cell size of *D. discoideum*,[38,41] it remains unclear on what timescale such acute cell volume changes are translated to the nucleus. To experimentally address this, we fluorescently labeled Ras-related nuclear protein Ran, nucleoporin Nup62, or histone H2B (Figure 1A) as nuclear size markers for fluorescence microscopy. Cell size decreased during hyper-OS and increased during hypoosmotic stress (hypo-OS) (Figure 1A). Concurrently, nuclei shrink and deform, or swell and round up (Figure 1A). To determine the timescale of these nuclear size changes, we combined live-cell fluorescence confocal microscopy and microfluidics, which allowed continuous imaging under controlled changes in osmotic conditions (Figures 1B, 1C, and S1; Videos S1 and S2). Upon osmotic stress, both cell and nuclear size changed on a second-to-minute timescale. In the time-lapse confocal stacks, the average cellular size decreased to 0.7-fold of its initial size during hyper-OS, a reduction of ~180 μm^3 in ~3 min (n = 12 cells for control and n = 9 cells for hyper-OS) (Figures 1B and S1A). The nuclear volume similarly decreased on average to 0.7-fold of its initial size ~4.3 μm^3 reduction in ~50 s (n = 9 cells for control and hyper-OS) (Figures 1B and S1B). Although both cytosolic and nuclear volumes decreased by a similar ratio, the adaptation of nuclear volume initially lagged behind but subsequently caught up at a slightly faster rate. During hypo-OS, the average cell size increased 1.7-fold, ~410 μm^3 increase in ~3 min (n = 7 cells for control and n = 6 for hypo-OS) (Figures 1B and S1A), and nuclei expanded 1.4-fold of the initial size, ~6.0 μm^3 increase in ~130 s (n = 15 cells for control and n = 17 cells for hypo-OS) (Figures 1C and S1B).

Stress-induced cellular volume changes prompt crowding and molecular rearrangements in cyto- and nucleoplasm

Its rapid volume adjustment makes *D. discoideum* an ideal model organism to investigate how molecular crowding or dilution acutely impact the cell's macromolecular organization, independent of longer-term transcriptional and proteomic responses. We thus set out to visualize the cellular ultrastructure and macromolecules at high resolution directly in cells by cryo-ET. For this, we vitrified cells by plunge freezing ~1 min after hyper- or hypo-OS application (Figure S2A). We then prepared cryo-focused ion beam (cryo-FIB) lamellae and targeted areas in the nuclear periphery for cryo-ET to capture nuclear and cytoplasmic regions

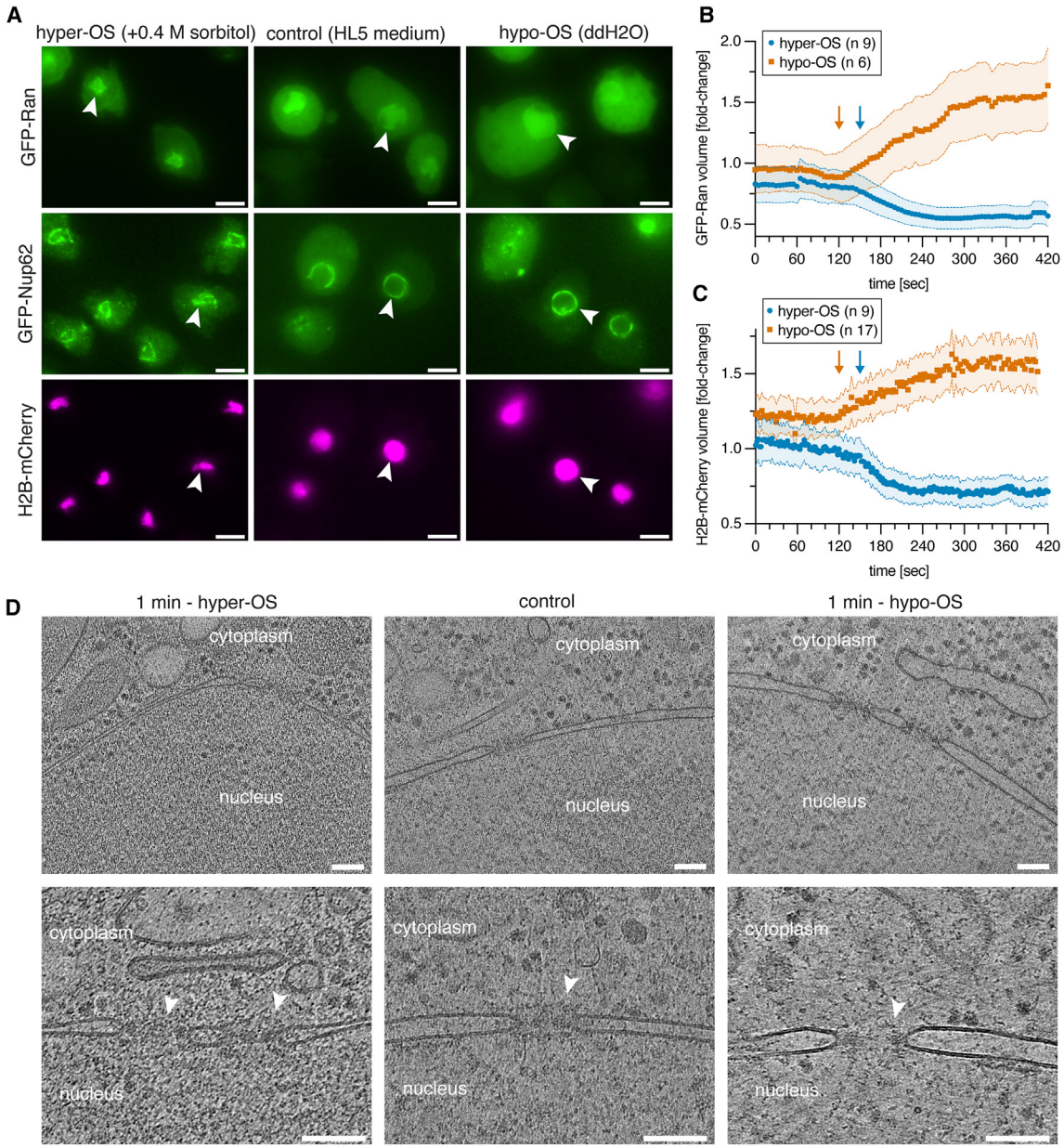

Figure 1. *D. discoideum* cells rapidly adapt to OS by changing cellular and nuclear size

(A) Live-cell fluorescence microscopy of cells overexpressing nuclear marker proteins GFP-Ran (top), or GFP-Nup62 (center) and H2B-mCherry (bottom) in control conditions (center) and after ~3 min of hyper-OS (left) or hypo-OS (right). Arrowheads highlight one nucleus in each panel.

(B) Fold-change of the cellular Ran-GFP volume during OS normalized control cell average.

(C) Fold-change of H2B-mCherry volume from confocal z stacks during OS normalized control cell average. SDEV shown as error margins. Time points of solution exchange (~150 s for hyper-OS; ~120 s for hypo-OS) in the microfluidics chamber are indicated by arrows (blue: hyper; orange: hypo).

(D) Slices of cryo-tomograms of control cells (center), and after applying ~1 min hyper-OS (left) or ~1 min hypo-OS (right). Cytoplasm and nucleus are labeled; white arrowheads indicate NPCs in the NE. Scale bars: 5 μm in (A) and 100 nm in (D).

(Figures 1D and S2A; Table S1). We compared these conditions to a control dataset of cells grown in HL5 medium (referred to as "control") prior to plunge freezing.[50] The tomographic data acquired after ~1 min of osmotic stress revealed clear differences in the cellular ultrastructure. While the cellular components and macromolecules in cyto- and nucleoplasm were more densely packed during hyper-OS, the contents appeared less crowded after hypo-OS (Figure 1D, and related cryo-tomograms EMD-52053, EMD-52054, EMD-52055). To quantify the effects on cytoplasmic protein concentrations and to quantify molecular crowding overall, we used ribosomes as a point of reference, as they are highly abundant and clearly identifiable in cryo-tomograms. Using

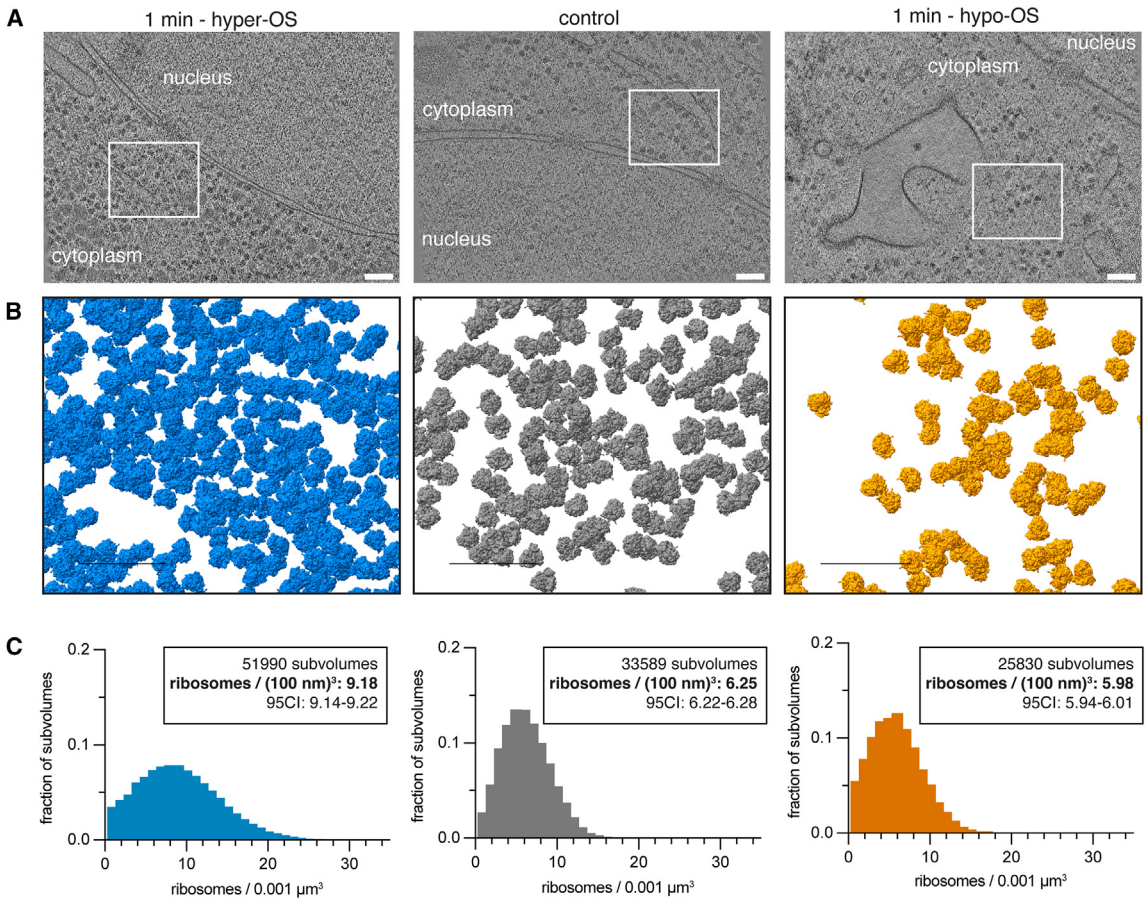

Figure 2. Osmotic stress rapidly affects cellular crowding

(A) Cryo-tomogram slice of cell after ~1 min of hyper-OS, in control conditions and after ~1 min of hypo-OS.

(B) Overview of ribosome positions determined by template matching (area indicated as white box in A).

(C) Histogram of the mean number of ribosomes in cytosolic subvolumes of $(100\ nm)^3$ around each identified ribosome position. The mean number and the 95% confidence interval (CI) displayed. Scale bars: 100 nm in (A) and (B).

a template matching approach[51] with the *D. discoideum* ribosome structure[50] (EMD-15808) as a template (Figure 2), we verified the positions of both cytosolic and membrane-bound ribosomes through classification.[50] We used ribosome numbers as a quantitative measure for cytosolic concentration changes (Figure 2B) and defined the number of ribosomes within a 100 nm box size (volume corresponds to 0.001 μm^3) around each ribosome position as an estimate for local cytosolic concentration (Figure 2C). The mean number of ribosomes per subvolume was 9.2 (51,990 subvolumes) under hyper-OS, 6.2 (33,589 subvolumes) in control cells, and 6.0 (25,830 subvolumes) under hypo-OS. The mean local concentration of ribosomes increased by about 50% from 10 to 15 µM during hyper-OS. The determined ribosome concentration changes correlate with the overall changes in cellular volume. Classification of ribosomes into different translation cycle states, as previously described for *D. discoideum* and other organisms,[50,52–54] revealed that translation continued under stress conditions, as the most populated states were present in all conditions. The largest proportion of states had P-site tRNA present, despite changes in cytoplasmic ribosome concentration (Figure S2B),[50] while some re-equilibration between different states was however apparent (Figure S2B). Increased molecular crowding was also evident for the cell nucleus, and a fraction of the analyzed nuclei (in 13 out of 52 cells) contained fiber-like arrangements (Figure S2C). While some repetitive features of this arrangement approximately matched the dimensions of nucleosomes (10–12 nm × 4–6 nm),[55] we were not able to obtain a conclusive subtomogram average.

The *D. discoideum* NPC architecture has a unique NR arrangement with a triple Y-complex configuration

To understand how the NPC scaffold adapts to different osmotic conditions and to precisely measure NPC diameters as a prerequisite for the quantification of flow, we first had to determine the *D. discoideum in situ* NPC structure. We did this by combining subtomogram averaging (STA) and integrative modeling of conserved architectural features. A total of 743 NPCs from all conditions combined were analyzed using STA based on previous processing workflows (Figures 3A, S2D, and S2E) (see STAR Methods). We identified, so far, non-annotated homologs using

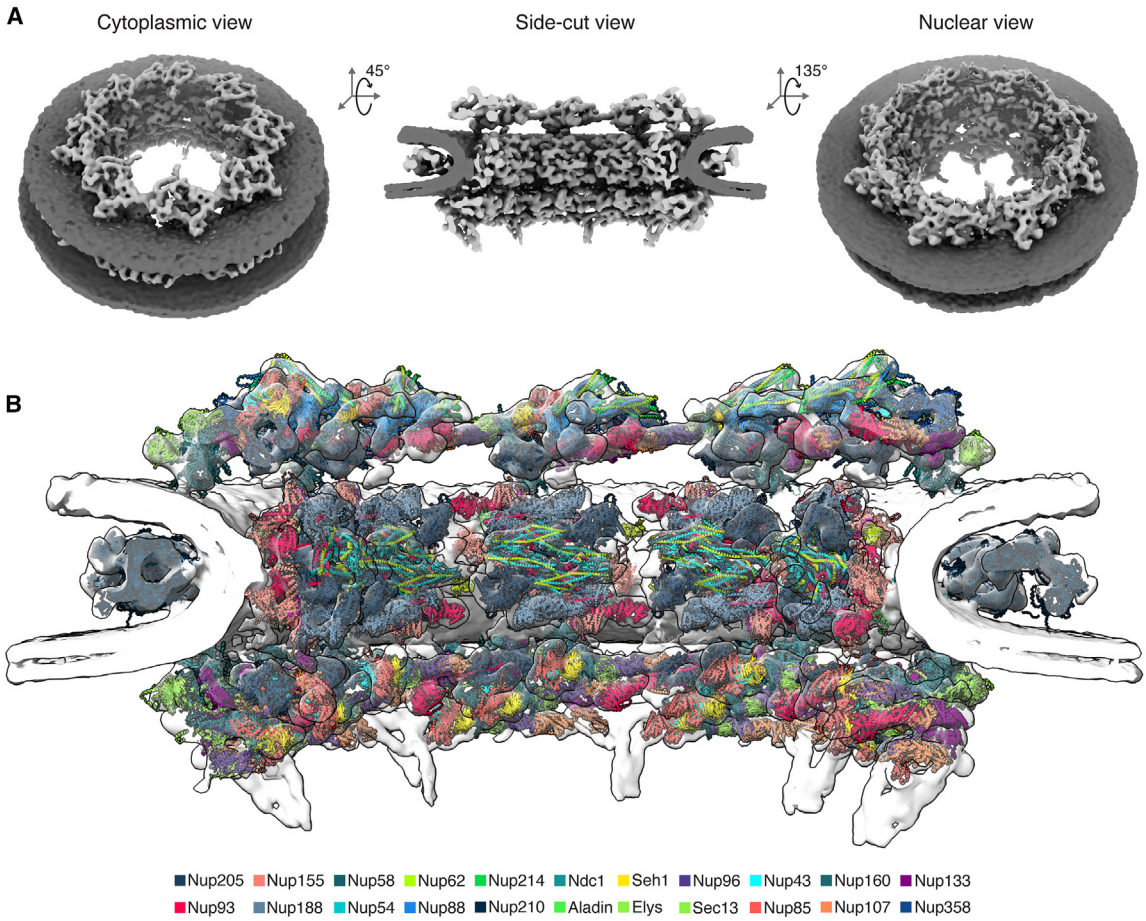

Figure 3. *In situ* structure of the *D. discoideum* NPC using STA and integrative modeling based on AlphaFold structural models

(A) STA map of the *D. discoideum* NPC as cytoplasmic view (left), side-cut view (center), and nuclear view (right). NPC scaffold (light gray), nuclear membrane (dark gray).

(B) Integrative structural model of the *D. discoideum* NPC scaffold built using AlphaFold models and STA density, and guided by the human NPC model.[13]

bioinformatics tools (Table S3) and built structural models for *D. discoideum* Nups and their interfaces using AlphaFold[56,57] (Figure S3; Table S3). To validate that the predicted *D. discoideum* Nups have the same fold as already known Nup homologs, we searched for similar folds in the PDB using Foldseek.[58] (Figure S4; Table S3) Fitting of *D. discoideum* Nup subcomplexes into the respective cryoelectron microscopy (cryo-EM) map allowed us to confidently assign the structured Nups to the overall scaffold (Figures 3B and 4A) (see STAR Methods). This revealed an unexpected and unique structural arrangement compared to previously published NPCs from other species, such as human, *S. pombe*, *S. cerevisiae*, *X. laevis,* or *C. reinhardtii*.[13–17,26,59,60]

The IR architecture was conserved compared to other organisms (Figure 4B1). Similarly, we observed density for a continuous luminal ring (LR), which fitted to the structural model of eight copies of the *D. discoideum* Nup210 homolog per spoke as seen in the human NPC (Figure 4B2). As in *C. reinhardtii* and *S. cerevisiae*, but in contrast to the human NPC, the CR was composed of a single ring of eight Y-complexes in head-to-tail arrangement (Figure 4B3). This ring was further decorated with density for one copy of the Nup205-Nup93 complex, two copies of the Nup214 complex, and two copies of Nup358 (Figures 4B3, S5C, and S5D). Clear density was present in the map for the *D. discoideum* Elys homolog (Figures 4C and S6). In contrast, Elys is not present at the human CR Y-complex.[13,14] However, there is structural evidence from *S. pombe* cells that its distant and much smaller Elys homolog is similarly present at both CR and NR,[26] while this protein is not conserved in *S. cerevisiae*.[61] The asymmetric distribution of Elys was preserved in *D. discoideum* NPCs; however, it was achieved through the asymmetric distribution of Y-complexes across rings. Interestingly and unique to all organisms for which the NPC has been structurally analyzed, the *D. discoideum* NR contained three concentric rings of stacked Y-complexes, accounting for 24 copies (Figures 4 and S2F). The inner and the central Y-complex were present in a head-to-tail arrangement. However, the outermost copy of the NR Y-complex was truncated and lacked density at the expected position of Nup133 (Figures 4B and S5). Instead, Nup133 and the interacting C-terminal domain of Nup107 (amino acid [aa] 708–985) from the outermost NR Y-complex could be

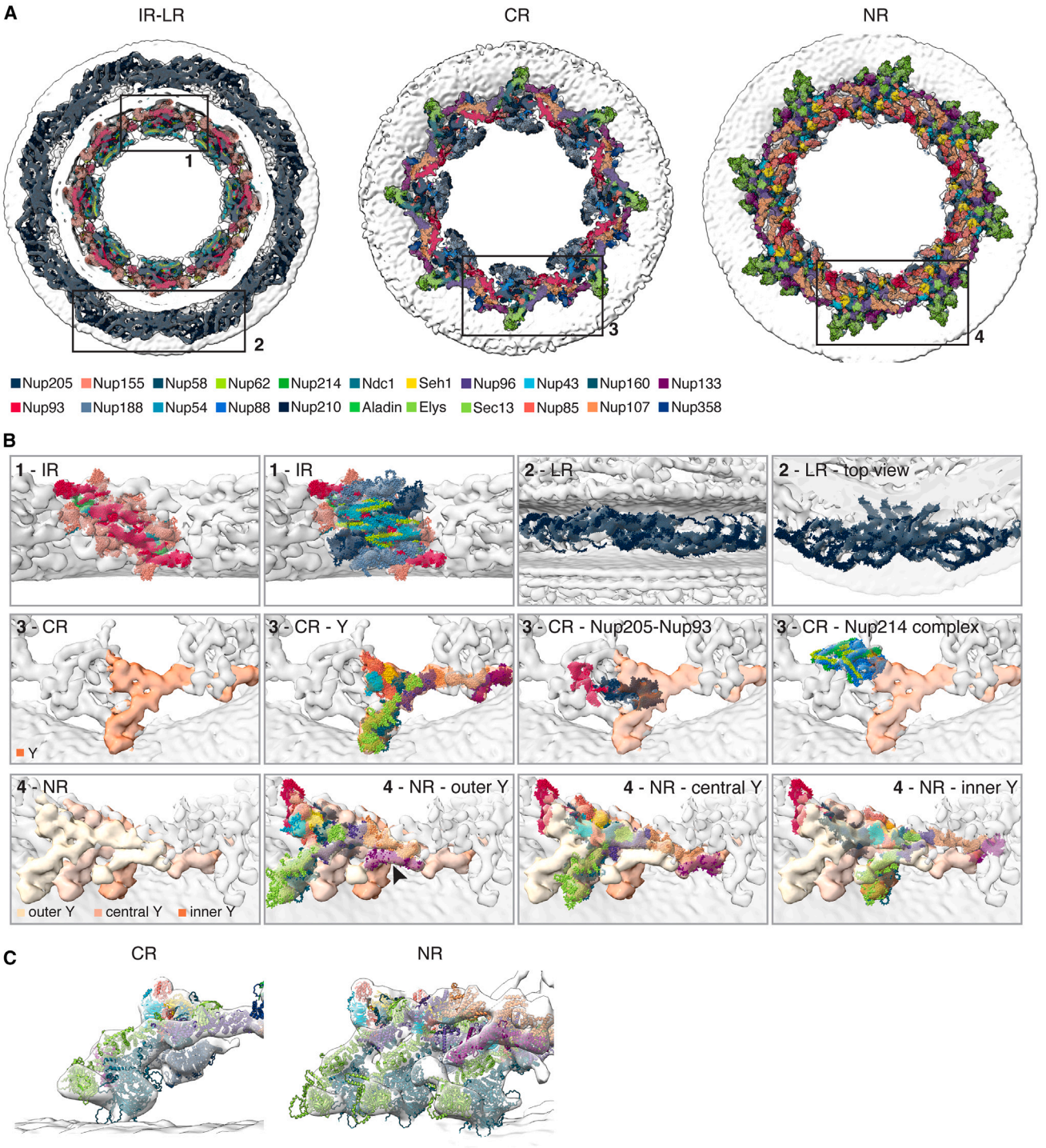

Figure 4. Structural arrangement of the *D. discoideum* NPC

(A) Structural overview of the inner ring (IR), luminal ring (LR) (left), cytosolic ring (CR) (center), and nuclear ring (NR) (right). IR and LR are shown as cut-view from cytoplasm.

(B) Top left: IR spoke with predicted AlphaFold models and only membrane-proximal Nups of IR (left). Top right: LR fitted with 8 copies of *D. discoideum* Nup210 homolog per asymmetric unit. Center row: CR contains one Y-complex (orange) per asymmetric unit. Highlighted are the Y-complex, Nup205-Nup93, and two

(legend continued on next page)

fitted into a neighboring unassigned density with high confidence (Figures S5B and S5E). This configuration requires a conformational rearrangement between the N- and C-terminal domains of Nup107. The unstructured insertion (aa 642–702) in the *D. discoideum* Nup107 structured fold may enable such conformational rearrangement (Figure S5F). Further validation will be necessary to investigate the molecular function of the observed Nup133 arrangement in the outer Y-complex and exactly how the head-to-tail arrangement of Y-complexes differs between the human and *D. discoideum* NPC (Figure S6). Additionally, the *D. discoideum* NR asymmetric unit contained one copy of the Nup205-Nup93 heterodimer and density for nuclear basket attachment (Figure 4B).

D. discoideum CR and NR scaffolds are resilient to stress-induced diameter changes

Previous work in *S. pombe* revealed that NPCs constrict under conditions of hyper-OS, when NE ruffling is observed. This led to the proposal that NE membrane tension regulates NPC diameter.[26] This model predicts that the relationship between osmotic pressure and NPC diameter is relevant for both hyper- and hypoosmotic conditions. The latter could not be tested in *S. pombe* cells because their cell wall prevents volume increase. To experimentally test the prediction in *D. discoideum*, we structurally analyzed NPCs after the application of hyper- or hypo-OS and compared them to control cells (Figures 5A and 5B). The diameter of the *D. discoideum* NPC was on average 72.8 nm in control cells. Confirming our prediction, we observed NPC dilation to 77.5 nm under hypoosmotic conditions, contrasting hyper-OS, where NPCs were constricted to 67.8 nm on average.

Overall, the *D. discoideum* NPC has a larger diameter compared to the human NPC (54 nm[13]) or the *S. pombe* NPC (68.8 nm[26]), but constriction changes are notably less pronounced, despite the extreme osmotic changes. NPC constriction and dilation movements were largely performed by the IR spokes, LR, and NE membrane (Figures 5C–5E; Video S3). While the position of the CR stayed fixed (Figure 5E), the NR underwent a tilting motion and moved closer to the IR spoke during hyper-OS (Figure 5A; Video S3), whereby the NR diameter remained constant (Figure 5D).

Previous mathematical modeling suggested that osmotic pressure, which inflates the NE lumen, and membrane tension acting on the NE can be described as equivalent to each other.[26] As a consequence, the distance between the inner nuclear membrane (INM) and outer nuclear membrane (ONM), as observed by cryo-ET, correlates with NPC diameter—a relationship that was experimentally validated in *S. pombe* cells for NPC constriction during hyper-OS.[26] To test whether NE thickness and NPC diameter are coupled in *D. discoideum* under osmotic stress, we systematically quantified changes in NE volume through NE segmentations (Figure 5F). The NE thickness was reduced during hyper-OS, while hypo-OS led to inflation, in alignment with our previously postulated model (Figure 5F). Indeed, NE thickness and the mean NPC diameter were positively correlated (Spearman correlation coefficient of 0.903) (Figure 5G). Taken together, these analyses provide direct experimental evidence for our model how NE tension regulates NPC diameter in an organism in which both NPC constriction and dilation can be directly captured.

Pressure-driven volume changes of the nucleus cause directional fluid flow across NPCs

To explain the observed rapid nuclear volume changes induced by the osmotic gradient, directional flow out of or into the cell and nucleus is required. For the nucleus, this flow can occur across the NE membranes for solvent or through the NPC central channel for solvent and ions. To approximate the flow that occurs across a single NPC, we first estimated the number of NPCs in *D. discoideum* by integrating our STA and NE segmentation data with the light microscopic data (see STAR Methods). The average NPC density was 14 NPCs/μm^2 (95% confidence interval [CI] between 10 and 17) in control, 15 NPCs/μm^2 (95% CI between 13 and 17) in hyper-OS, and 9 NPCs/μm^2 (95% CI between 8 and 10) in hypo-OS conditions (Figure 5H). From confocal microscopy stacks (Figure 1), we determined the mean nuclear volume to ~20 μm^3 (n = 50 cells) in control cells and ~26 μm^3 (n = 17 cells) during hypo-OS. As a result, *D. discoideum* cells have about 380 to 540 NPCs (see STAR Methods). This is more than previously estimated for budding yeast (100–200 NPCs),[62] but fewer than estimated for human hepatocytes or U-2 OS cells (2,000 NPCs with 14–16 NPCs/μm^2 [63] or 3,000 NPCs, respectively[64]).

In our estimation of the osmotic imbalance-driven fluid flow across the NE, we account for water passage through the semi-permeable lipid membranes and for the flow of solvents, including osmolytes through the NPCs. We integrated our experimental data into a mathematical model of hydrodynamics across NPCs to quantify the fluid flow required for nuclear volume adjustments (Figures 6A and 6B) and derive the permeability of the NPC central channel. Considerations and simplifying assumptions in our model are laid out in detail in STAR Methods. Those are, in brief, an idealized spherical shape for the cell and nucleus, a previously determined water permeability for the biological membranes,[65,66] and rapid mixing via Fickian diffusion within the cytoplasmic and nuclear compartments. In our assessment, the largest uncertainty is the unknown lipid composition of the nuclear membranes, for which we consider the lipid composition of the ER and experimental studies on its permeability, suggesting that it is considerably higher compared to the plasma membrane (PM).[66–70] We assessed the robustness of our model to this uncertainty by considering a range of 35–700 $\mu m \cdot s^{-1}$ for the NE permeability, referred to as "uncertainty range" below. Taking these considerations into account, four tightly coupled differential equations for the four time-dependent variables (concentrations and radii of cytoplasm and nucleus) were obtained (see STAR Methods). The differential equations are solved numerically for cells experiencing hyper-OS (Figures 6C–6E) and hypo-OS (Figure S7):

copies of the Nup214 complex. Bottom row: three Y-complexes form the structural building block of the NR asymmetric unit. One copy is located close to the nuclear membrane (orange), one in the center (light orange), and a shorter outer Y-complex (yellow) with non-canonical conformation of Nup133 (arrowhead; see Figure S5). Each Y-complex and Nup205-Nup93 are highlighted.
(C) Views on the membrane attachment of the long arm of *D. discoideum* Y-complexes in CR (left) and NR (right).

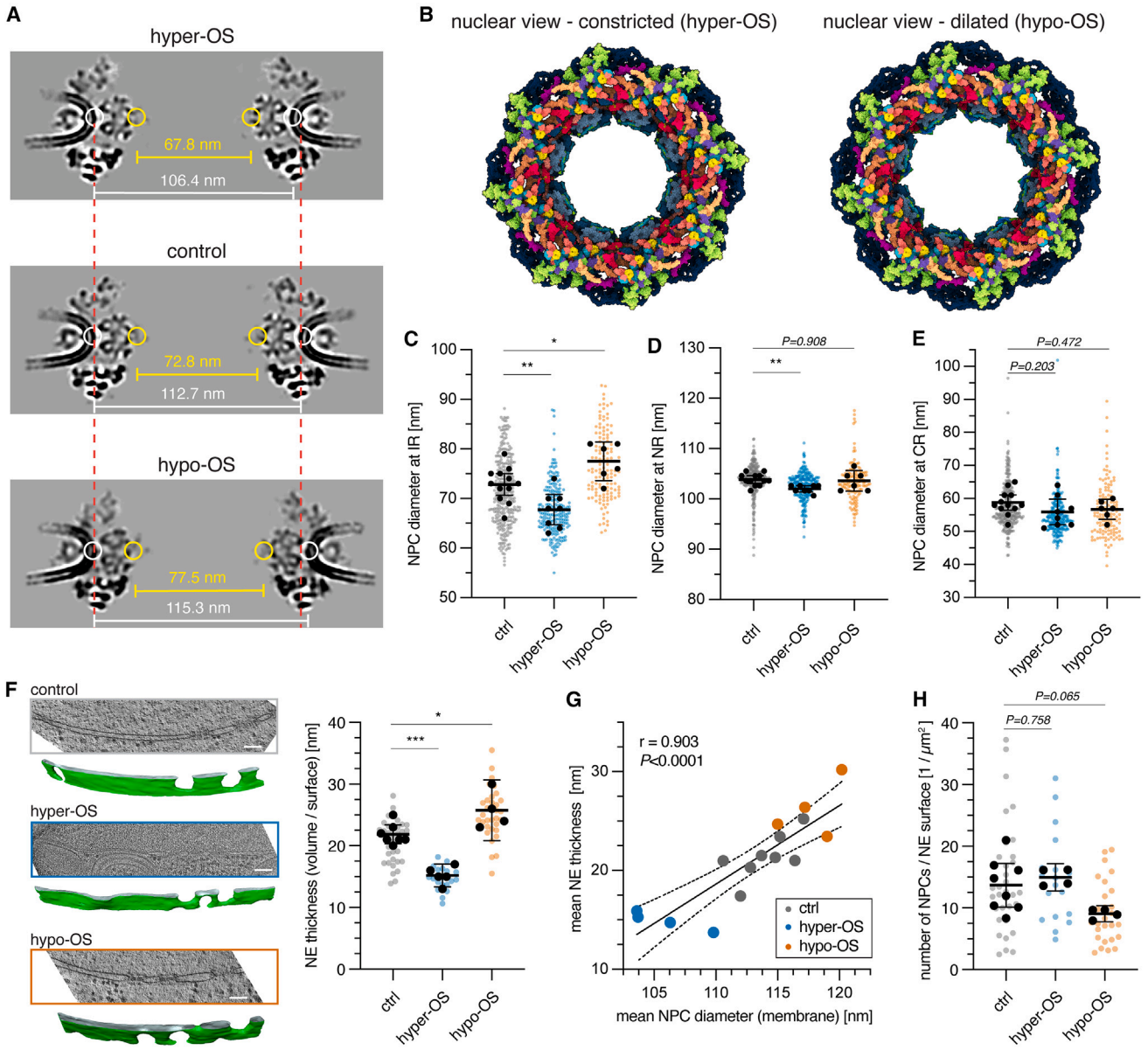

Figure 5. Osmotically induced constriction and dilation of *D. discoideum* NPCs are coupled to NE thickness and mediated by movement of the nuclear membrane and IR spokes, while the NR and CR remain rigid

(A) STA maps of constricted NPCs (hyper-OS), in control conditions and dilated NPCs (hypo-OS). Mean diameter between IR spoke shown in yellow and between the outer leaflet of nuclear membrane in white. The red dashed line indicates the membrane distance under control conditions for comparison.

(B) Constricted and dilated NPC scaffold under hyper-OS (left) and hypo-OS (right) (subunit coloring as in Figure 3B).

(C) NPC diameter between IR spokes (control: mean diameter = 72.8 nm, 95% CI [70.7, 75.0], *n* = 12 grids, hyper-OS: mean diameter = 67.8 nm, 95% CI [64.7, 70.8], *n* = 8 grids and hypo-OS: mean diameter = 77.5 nm, 95% CI [73.6, 81.4], *n* = 6 grids).

(D) NPC diameter between NR subunits (control: mean diameter = 104.3 nm, 95% CI [103.5, 105.0], *n* = 12 grids, hyper-OS: mean diameter = 102.4 nm, 95% CI [101.8, 103.0], *n* = 8 grids and hypo-OS: mean diameter = 104.0 nm, 95% CI [101.9, 106.1], *n* = 6 grids).

(E) NPC diameter between CR subunits (control: mean diameter = 58.8 nm, 95% CI [56.5, 52.0], *n* = 12 grids, hyper-OS: mean diameter = 55.9 nm, 95% CI [52.0, 59.8], *n* = 8 grids and hypo-OS: mean diameter = 56.7 nm, 95% CI [53.7, 59.7], *n* = 6 grids).

(F) Segmentation of NE from tomograms (left) and quantification of NE volume to surface area (right) as approximation for NE thickness (control: mean thickness = 21.9 nm, 95% CI [20.3, 23.4], *n* = 7 grids, hyper-OS: mean thickness = 15.2 nm, 95% CI [13.4, 17.0], *n* = 5 grids and hypo-OS: mean thickness = 25.8 nm, 95% CI [20.8, 30.7], *n* = 4 grids). Scale bar: 100 nm.

(legend continued on next page)

Under hyper-OS, we obtained the best fit to our confocal microscopy data (Figures 1B, 1C, and S1) for a permeability coefficient of $k_{NPC_w} \sim 49.2\ nm^3/(Pa \cdot s)$(uncertainty range: 23.1–92.3) for a single NPC. Translated into fluid flow across the central channel of one NPC, this equates to $\sim 4.5 \times 10^{-4}\ \mu m^3 s^{-1}$ for a concentration gradient of 0.2 mM across the NE. For reference, the volume contained within the central channel of a single NPC is about $5 \times 10^{-4}\ \mu m^3$.

The permeability barrier remains intact during fluid flow across NPCs

The central channel of the NPC is, however, not empty but densely packed with FG-Nups. Considering the estimated flow rates, we wondered if the permeability barrier for macromolecules also remains intact under acute osmotic stress conditions. The tomographic data indicated no mixing of observable nuclear and cytosolic features: ribosomes did not leak into the nucleus under conditions of hypo-OS, nor did chromatin migrate into the cytosol subsequent to hyper-OS. We additionally experimentally tested NE permeability barrier integrity for larger macromolecules with 500 kDa fluorescein isothiocyanate (FITC)-dextran, which did not enter the nucleus following acute nuclear volume increase during PM lysis under hyper-OS (Figures S7A and S7B). Together, these observations indicated that the FG-Nup mesh inside the central channel remains intact and, importantly, that *D. discoideum* nuclei did not rupture during rapid nuclear volume changes.

Porous flow model for fluid flow across NPCs during hyperosmotic shock

Having established the NPC permeability coefficient and confirmed that the NE barrier function stays intact, the effective pore size of the NPC can be estimated. Using the Hagen-Poiseuille law for pipe flow, we converted the estimated permeability coefficient of $k_{NPC_w} \sim 49.2\ nm^3/(Pa \cdot s)$ for a single NPC under hyperosmotic conditions into an effective radius of $\sim$ 3.3 nm (uncertainty range: 2.8–3.9 nm) for a single $\sim$100-nm long tube and a solvent viscosity μ about 10 times that of water.[71,72] However, models of fluid flow through a porous medium based on Darcy's law[73–77] may offer a more realistic description of fluid passage through the dynamic network of FG-Nups in the NPC central channel.[12,78–80] In this case, we could relate the permeability coefficient of k_{NPC_w} to the porous medium permeability coefficient k_{Darcy} (STAR Methods), and in turn, estimate an effective radius of the fluid pores using the NPC geometry and the solvent fraction in the pore as additional inputs. For hyper-OS, we obtain $k_{Darcy} \sim 0.012\ nm^2$ (uncertainty range: 0.006–0.024 nm^2), resulting in a critical radius r_{CR} of flow tubules ranging from $\sim$0.12 to 0.15 nm (uncertainty range: 0.08–0.22 nm) for porous channels in the homogeneous media, wide enough for water passage (Figure 6F, blue).

Flow and NPC diameter are interdependent

Under hypo-OS, modeling is complicated by the buildup of tension in the NE caused by swelling of the nucleus. By setting the tension factor to $\sigma_{NE} = 0.05\ Nm^{-1}$, a value obtained by equating the osmotic pressure to the tension-related hydrostatic pressure,[81] we estimate a permeability coefficient of $k_{NPC_w} \sim 148\ nm^3/(Pa \cdot s)$ for a single NPC during hypo-OS (Figure S7D). Our results thus indicate a fluid flow across the central channel of the NPC that is $\sim$3 times larger compared to the hyper-OS condition. For the Hagen-Poiseuille model with a single cylindrical central opening, we obtain an effective tube radius of $\sim$4.41 nm (uncertainty range: 2.90–5.55 nm), and for the porous flow model, the effective tubule radius is $\sim$0.21–0.27 nm (uncertainty range: 0.08–0.40 nm) during hypo-OS (Figure 6F, orange). This increased permeability is in accord with the increased NPC central channel diameter (Figures 5A and 5B). Our results imply that NPC dilation and constriction affect central channel permeability and the osmotic response of the nucleus.

Viral NPC blockage decreases nuclear size response

We predict that altering the NPC number or blocking the central channel should similarly affect the osmotic response of the nucleus. As experiments in *D. discoideum* altering NPC numbers or blocking the central channel are technically challenging, we turned to studying the nuclear size response during hypo-OS in HEK293 cells. These cells transiently express GFP-tagged SARS-CoV-2 protein Orf6, which previous studies found to interact with Nup98 and Rae1 at the NPC, thereby blocking mRNA export and nucleocytoplasmic trafficking.[82–84] In line with our prediction, cells overexpressing high levels of Orf6-GFP had a slower nuclear size response upon hypo-OS compared to non-transfected control cells. This indicates that reduced NPC permeability affects the initial response, while equilibration to a similar nuclear size fold-change occurred after 5–10 min of osmotic stress (Figures 6G and 6H). Overall, these results provide additional evidence that fluid flow across NPCs can be modulated and may play an important role in the stress response to environmental changes.

DISCUSSION

In our study, we solve the *in situ* structure of the *D. discoideum* NPC at 23–32 Å resolution. At this resolution, major NPC scaffold subcomplexes and their higher order structure are resolved and thus built into our model of the *D. discoideum* NPC. We show that NPCs can undergo both constriction and dilation when osmotic stress is applied. Solving the NPC structure directly in cells is critical to differentiate between NPC dilation and possible rupture events, which may occur under certain stress conditions.[85,86] Surprisingly, our structural analysis shows that *D. discoideum* NPCs have an elaborate scaffold with three concentric Y-complex rings on the nuclear side and one on the

(G) NE thickness plotted against the mean NPC membrane diameter for each grid of control cells, during hyper-OS and hypo-OS. Spearman correlation: r = 0.903 and $p < 0.0001$. Linear regression plotted with 95% CI as black line. Data points for controls: gray; hyper-OS: blue; hypo-OS: orange.
(H) Mean number of NPCs per NE surface area (control: mean number per μm^2 = 13.7, 95% CI [10.1, 17.2], n = 8 grids, hyper-OS: mean number = 15.0 nm, 95% CI [12.8, 17.2], n = 4 grids and hypo-OS: mean number = 9.1 nm, 95% CI [7.8, 10.4], n = 4 grids). Statistical significance was tested using ordinary one-way ANOVA, significance level: $^*p < 0.05$, $^{**}p < 0.01$, $^{***}p < 0.001$, p values are stated for non-significant results.

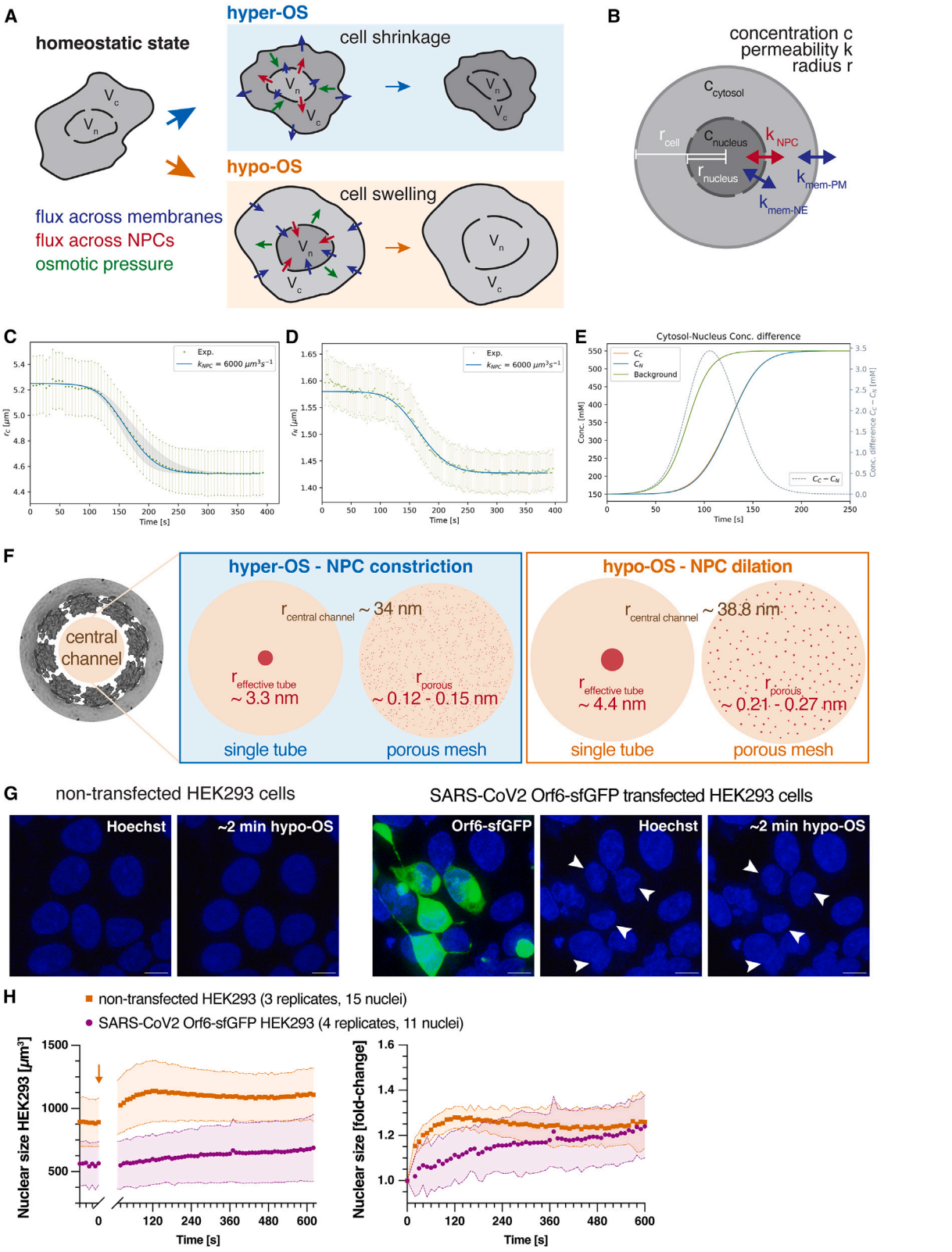

(legend on next page)

cytoplasmic side. This scaffold stoichiometry differs from previously assessed organisms[87] and adds to the structural diversity of NPCs that can assemble from evolutionarily conserved Nups into functional NPCs. In contrast to *S. pombe* and human cells,[13,26] *D. discoideum* NPC diameter adaptations are limited to movements of the IR spoke, LR, and the NE membrane. The *D. discoideum* CR and NR scaffold structures are remarkably immobile to overall constriction and dilation movements. Besides the notable three Y-complex rings of the NR, which may provide additional rigidity to the scaffold, Nup133 attaches in a different position and may contribute to the observed rigidity of CR and NR in *D. discoideum*. Furthermore, additional copies of Nup155, which connect the NR and CR to the IR spoke in human and *S. pombe* NPCs, are missing in *D. discoideum*, which might restrict translation of movement from the IR and membrane to the NR and CR. The more detailed structural interfaces important for NPC dilation and constriction remain to be investigated.

The current view on nucleocytoplasmic transport knows two mechanisms for the translocation of molecules across NPCs: passive diffusion and active transport. Passive diffusion allows macromolecules smaller than 30–60 kDa to diffuse in equilibrium between the nucleus and cytoplasm. In contrast, active transport requires binding of a transport receptor to the cargo molecules, as well as the RanGTP gradient, to facilitate movement through the FG-mesh of the central channel.[5–7,88] The concept of porous flow presented here is a functionally distinct translocation mechanism, because it is dependent on acute changes to physical pressure. Specifically, cellular solvents directionally flow across NPCs in response to a gradient or force, while the permeability barrier function to macromolecules remains intact.

In line with and building on previous models for nuclear-to-cell size control,[46,47] we show that volume equilibration processes during osmotic stress in *D. discoideum* result in nuclear size adaptation. Our mathematical model based on hydrodynamic principles estimates the magnitude of the associated fluid flow, with rates greater than the complete central channel volume each second. Using this model, we calculated an effective channel opening or effective pore size that is available for fluid flow in the central channel of the NPC. At the same time, the central channel is not empty but contains a high concentration of FG-Nups, cargo, and transport factors,[79,89] additionally restricting free flow of solvent. Our model predicts the permeability of *D. discoideum* NPCs to cellular fluid. It indicates that the bottleneck for *D. discoideum* cells during the osmotic volume adaptation is the flow across the PM and that nuclear volume adaptation is not restricted by flow across the NE. However, our model is limited by its largest factor of uncertainty: the permeability of the NE membrane, which needs to be inferred from parameters of other cellular membranes. Aquaporins, ion channels, and lipid compositions are unknown contributing factors to NE permeability.[49,90,91] In cells, the scenario is even further complicated by multiple parameters, and thus the physiological implications of porous flow remain to be tested in the future. In addition, the FG-Nup density may not be distributed homogeneously in the central channel. A proposed reduction at its center[11,12,92,93] would result in profound effects on central channel permeability. Critical NPC diameters that allow for central openings in reconstituted synthetic pores range between 60 and 80 nm[94] and are compatible with the NPC diameter range we observe *in situ* for *D. discoideum*. Inside cells, however, changing osmolarity may also affect the local FG-Nup concentration, similar to the general crowding effects that we observed in cytosol and nucleoplasm. Possible changes in cohesion and molecular condensation behavior may significantly influence FG-Nup arrangement and consequently solvent permeability and fluid flow. Given these limitations, we provide an uncertainty range in our model. Despite this, it is important to note that our calculated NPC effective pore radius according to Hagen-Poiseuille is indeed compatible with the size range of macromolecules that can undergo passive diffusion.[8] Therefore, we believe that our model reflects an appropriate estimate for fluid flow when osmotic stress is applied to *D. discoideum* cells. Overall, our model for fluid flow, taken together with the well-established permeability barrier for macromolecules, best fits with a central channel that contains one or few openings and that varies with a changing NPC diameter. In such a scenario, the remaining fluid flow may be achieved through the porous, dynamic FG medium.

An intriguing hypothesis is that NPC dilation and constriction may regulate the flow across the NPC central channel during

Figure 6. Model for porous flow across the central channel of NPCs

(A) Cellular and nuclear volume adjustments during acute osmotic stress. Osmotic pressure causes cell swelling in the case of hypo-OS and cell shrinkage for hyper-OS.

(B) Schematic model of idealized spherical cell and nucleus assumed for model calculations, with the radii (r) and osmolyte concentrations (c) of cell and nucleus matched to volumetric measurements during osmotic shock.

(C and D) Experimental and theoretically predicted time-dependent cell radius (C) and nucleus radius (D) for hyper-OS. Gray lines in C show the theoretical predictions for the PM permeability $k_{mem\text{-}PM}$ of 30 and 40 $\mu m \cdot s^{-1}$.

(E) Theoretically predicted time-dependent concentrations of cyto- and nucleoplasm for hyper-OS. Shown on vertical axis (gray; dashed line) is the difference between the predicted concentrations.

(F) Schematic display of central channel permeability from mathematical models during hyper- and hypo-OS based on fitting to experimental data. Left schematic shows the effective channel size radius of ~3.3 nm for hyper-OS if one continuous single path through the FG-mesh is assumed according to Hagen-Poiseuille law (model 1). Model 2 shows the FG-mesh as a homogeneous porous mesh with a critical radius of ~0.12–0.15 nm for hyper-OS according to Darcy's law (blue). For hypo-OS (orange), the effective channel size radius equates to ~4.4 nm (model 1) and ~0.21–0.27 nm (model 2).

(G) Maximal intensity projections of nuclei of non-transfected HEK293 cells (left) and of nuclei after ~48 h of transfection with SARS-CoV-2 Orf6-sfGFP (right) before and after ~2 min of hypo-OS. White arrows indicate nuclei of cells with high expression levels of Orf6-sfGFP selected for quantification. Scale bars: 10 μm.

(H) Quantification of nuclear size before and after application of hypo-OS (time point indicated by an orange arrow) for non-transfected HEK293 cells and cells expressing SARS-CoV-2 Orf6-sfGFP after 48 h (left). Nuclear size fold-change of the same cells normalized to untreated nuclear size (right). Mean and SD are shown.

stress conditions. Indeed, using our model of fluid flow across NPCs, we can link lower flow across NPCs in hyper-OS to constricted NPCs and higher flow during hypo-OS to dilated NPCs. Thus, the permeability of the central channel to cellular solvent changes with the changing NPC diameter. Like a self-regulating valve, NPCs may allow for more fluid flow under conditions when nuclei expand under mechanical stress, thus relieving stress. We showed that *D. discoideum* nuclei are sufficiently robust to withstand osmotic stress without impairment of the NPC barrier function for large macromolecules. However, to efficiently relieve osmotic stress through fluid flow and prevent nuclear rupture, cells likely must operate within a defined range of NPC permeability. Consequently, mutations affecting the number of NPCs, their distribution on the NE, or central channel FG properties[95–97] could affect nuclear permeability and alter the cells' resilience to osmotic stress. We provide indications that blockage of the NPC central channel may slow the nuclear size response to hypo-OS. However, future studies are required to consolidate the relevance of flow across NPCs in a physiological cellular context.

The strength of our approach is that the estimation of fluid flow across NPCs is directly based on experimental data. We integrate results from live-cell fluorescence microscopy and cryo-ET into a mathematical model that advances the understanding of a fundamental biophysical process as it occurs in cells. Since our proposed mechanism is directly linked to acute nuclear volume adaptations by stress-generated forces, it is likely important not only for cells that are highly adapted to osmotic stress, such as *D. discoideum*. The proposed concept of fluid flow across NPCs may be broadly applicable to cellular processes involving temporal nuclear shape changes. Such processes may include migrating cells, infiltrating cancerous cells, or cells subjected to mechanical forces in developing tissues.[98–101]

Limitations of the study

In situ cryo-ET of NPCs is limited in its currently achievable resolution. Our homology model of the *D. discoideum* NPC is less elaborate than recent human NPC models[13–15] and is based on integrative modeling of large, conserved subcomplexes. Together, this does not allow a detailed interpretation of the *D. discoideum* molecular interfaces between Nups without further biochemical validation. Approaches that can achieve higher resolution structures utilize NPCs in isolation and in a constricted state. Since a major focus of this research was the NPC scaffold and its dilation mechanism directly upon cellular perturbation, *in situ* cryo-ET is the only method suited for this purpose. As outlined above, our mathematical model is based on several assumptions; the resulting uncertainty is addressed by providing an uncertainty range for the interpretation of our mathematical model. Overexpression of SARS-CoV-2 GFP-Orf6 can be considered an artificial approach to manipulate NPC function, and while the observed slower osmotic response is in line with our model of reduced permeability, we cannot rule out potential secondary effects due to altered cell physiology. Developing means of blocking NPCs without affecting nuclear size or NPC number remains challenging, but will be important for directly perturbing NPC permeability in the future.

RESOURCE AVAILABILITY

Lead contact

Further information and requests for resources and reagents should be directed to the lead contact, Martin Beck (martin.beck@biophys.mpg.de).

Materials availability

All materials of this study are available upon request.

Data and code availability

- Filtered, bin4 tomograms, as presented in Figure 1B, are available at EM Data Bank: EMD-52053, EMD-52054, and EMD-52055. The modeled *D. discoideum* NPC structure is available at PDB: 9HCJ. The NPCs maps reported in this paper are available through the EM Data Bank with accession codes EMD-19137, EMD-19139, EMD-19140, EMD-19141, EMD-19142, EMD-19143, EMD-19144, EMD-19149, EMD-19152, EMD-19155, EMD-19156, EMD-19157, EMD-19158, EMD-51989, EMD-51990, EMD-51991, EMD-51992, EMD-51993, EMD-51994, EMD-51995, EMD-51996, EMD-51997, EMD-51998, EMD-51999, EMD-52000, EMD-52001, EMD-52002, and EMD-52003. 80S ribosome maps for hyper-OS and hypo-OS are available through EMD-52057 and EMD-52058. The raw tilt series data and alignment files for control, hyper-OS, and hypo-OS conditions are available through EMPIAR-11845, EMPIAR-11943, and EMPIAR-11944, respectively. Fluorescence microscopy data used for quantification are available through Zenodo (https://doi.org/10.5281/zenodo.14142946). These data are publicly available as of the date of publication.
- This paper does not report original code.
- Any additional information required to reanalyze the data reported in this paper is available from the lead contact upon request.

ACKNOWLEDGMENTS

We thank Christian Zimmerli, Matteo Allegretti, Reiya Taniguchi, Huaipeng Xing, Max Seidel, Iskander Khusainov, Florian Wilfling, and Maziar Heidari for advice and reagents. We thank Stefanie Böhm for careful reading and advice during manuscript preparation. We thank Sonja Welsch, Mark Linder, and the Central Electron Microscopy Facility of the Max Planck Institute of Biophysics for technical support and support with data acquisition. We thank Özkan Yildiz, Juan F. Castillo Hernandez, Thomas Hoffmann, and the Max Planck Computing and Data Facility for support with scientific computing. H.K. thanks International Max Planck Research School (IMPRS) on cellular Biophysics and the Max Planck Society.

This work was supported by the European Union (ERC, NPCvalve, project number 101054823 to M.B.). P.C.H. was supported by an EMBO Postdoctoral Fellowship (ALTF 33-2021). M.B. and G.H. acknowledge funding by the Max Planck Society. This research was also supported by the German Research Foundation (CRC 1507—Membrane-associated Protein Assemblies, Machineries, and Supercomplexes; Project 17 to M.B. and P12 to G.H.). L.C. acknowledges support from a research fellowship from the EMBL Interdisciplinary Postdoc (EIPOD) (MSCA-COFUND-FP: 29200900). S.C.-L., M.B., G.H., and B.T. acknowledge funding by the Chan Zuckerberg Initiative DAF, an advised fund of Silicon Valley Community Foundation (grant 2021-234666). H.K. and G.H. acknowledge financial support by the Clusterprojekt ENABLE funded by the Hessian Ministry for Science and the Art.

AUTHOR CONTRIBUTIONS

P.C.H. conceived the project, designed experiments, performed experiments, analyzed data, and wrote the manuscript; H.K. developed the mathematical model, analyzed data, and wrote the manuscript; A.O.-K. performed structural modeling, analyzed data, and wrote the manuscript; J.P.K. and E.A.-F. performed ribosome classification, analyzed data, and edited the manuscript; L.C. performed bioinformatical analysis under supervision of J.K.; L.C. and J.K. edited the manuscript; E.M. generated reagents and edited the manuscript; B.T. and S.C.-L. supported data processing and edited the manuscript;

G.H. and M.B. conceived the project, supervised the project, acquired funding, and wrote the manuscript.

DECLARATION OF INTERESTS

The authors declare no competing interests.

STAR★METHODS

Detailed methods are provided in the online version of this paper and include the following:

- KEY RESOURCES TABLE
- EXPERIMENTAL MODEL AND STUDY PARTICIPANT DETAILS
- METHOD DETAILS
  - Molecular biology and cell culture
  - Fluorescence Microscopy
  - Cell and nuclear size determination
  - Cryo-EM sample preparation
  - Cryo-ET acquisition
  - Tomogram reconstruction
  - Ribosome template matching
  - Ribosome classification and ribosome analysis
  - NPC particle selection and subtomogram averaging
  - NPC diameter measurements
  - NE segmentation, NPC diameter correlation and NPC density calculation
  - Bioinformatics identification of *D. discoideum* Nups
  - Structural modeling of Nups and NPC subcomplexes
  - Fitting of atomic structures to cryo-ET maps
  - Systematic fitting
  - Modeling of the *D. discoideum* NPC scaffold
  - Mathematical model of fluid flow across the NPC and NE during osmotic stress
  - Porous flow model
  - Uncertainty estimation
- QUANTIFICATION AND STATISTICAL ANALYSIS

SUPPLEMENTAL INFORMATION

Supplemental information can be found online at https://doi.org/10.1016/j.molcel.2024.11.038.

Received: February 7, 2024
Revised: August 16, 2024
Accepted: November 27, 2024
Published: December 26, 2024

REFERENCES

1. Knockenhauer, K.E., and Schwartz, T.U. (2016). The Nuclear Pore Complex as a Flexible and Dynamic Gate. Cell *164*, 1162–1171. https://doi.org/10.1016/j.cell.2016.01.034.
2. Hampoelz, B., Andrés-Pons, A., Kastritis, P., and Beck, M. (2019). Structure and Assembly of the Nuclear Pore Complex. Annu. Rev. Biophys. *48*, 515–536. https://doi.org/10.1146/annurev-biophys-052118-115308.
3. Lin, D.H., and Hoelz, A. (2019). The Structure of the Nuclear Pore Complex (An Update). Annu. Rev. Biochem. *88*, 725–783. https://doi.org/10.1146/annurev-biochem-062917-011901.
4. Beck, M., and Hurt, E. (2017). The nuclear pore complex: understanding its function through structural insight. Nat. Rev. Mol. Cell Biol. *18*, 73–89. https://doi.org/10.1038/nrm.2016.147.
5. Schmidt, H.B., and Görlich, D. (2016). Transport Selectivity of Nuclear Pores, Phase Separation, and Membraneless Organelles. Trends Biochem. Sci. *41*, 46–61. https://doi.org/10.1016/j.tibs.2015.11.001.
6. Görlich, D., and Mattaj, I.W. (1996). Nucleocytoplasmic Transport. Science *271*, 1513–1518. https://doi.org/10.1126/science.271.5255.1513.
7. Wente, S.R., and Rout, M.P. (2010). The nuclear pore complex and nuclear transport. Cold Spring Harb. Perspect. Biol. *2*, a000562. https://doi.org/10.1101/cshperspect.a000562.
8. Mohr, D., Frey, S., Fischer, T., Güttler, T., and Görlich, D. (2009). Characterisation of the passive permeability barrier of nuclear pore complexes. EMBO J. *28*, 2541–2553. https://doi.org/10.1038/emboj.2009.200.
9. Keminer, O., and Peters, R. (1999). Permeability of single nuclear pores. Biophys. J. *77*, 217–228. https://doi.org/10.1016/S0006-3495(99)76883-9.
10. Paine, P.L., Moore, L.C., and Horowitz, S.B. (1975). Nuclear envelope permeability. Nature *254*, 109–114. https://doi.org/10.1038/254109a0.
11. Kozai, T., Fernandez-Martinez, J., van Eeuwen, T., Gallardo, P., Kapinos, L.E., Mazur, A., Zhang, W., Tempkin, J., Panatala, R., Delgado-Izquierdo, M., et al. (2023). Dynamic molecular mechanism of the nuclear pore complex permeability barrier. Preprint at bioRxiv. https://doi.org/10.1101/2023.03.31.535055.
12. Yu, M., Heidari, M., Mikhaleva, S., Tan, P.S., Mingu, S., Ruan, H., Reinkemeier, C.D., Obarska-Kosinska, A., Siggel, M., Beck, M., et al. (2023). Visualizing the disordered nuclear transport machinery in situ. Nature *617*, 162–169. https://doi.org/10.1038/s41586-023-05990-0.
13. Mosalaganti, S., Obarska-Kosinska, A., Siggel, M., Taniguchi, R., Turoňová, B., Zimmerli, C.E., Buczak, K., Schmidt, F.H., Margiotta, E., Mackmull, M.T., et al. (2022). AI-based structure prediction empowers integrative structural analysis of human nuclear pores. Science *376*, eabm9506. https://doi.org/10.1126/science.abm9506.
14. Bley, C.J., Nie, S., Mobbs, G.W., Petrovic, S., Gres, A.T., Liu, X., Mukherjee, S., Harvey, S., Huber, F.M., Lin, D.H., et al. (2022). Architecture of the cytoplasmic face of the nuclear pore. Science *376*, eabm9129. https://doi.org/10.1126/science.abm9129.
15. Petrovic, S., Samanta, D., Perriches, T., Bley, C.J., Thierbach, K., Brown, B., Nie, S., Mobbs, G.W., Stevens, T.A., Liu, X., et al. (2022). Architecture of the linker-scaffold in the nuclear pore. Science *376*, eabm9798. https://doi.org/10.1126/science.abm9798.
16. Zhu, X., Huang, G., Zeng, C., Zhan, X., Liang, K., Xu, Q., Zhao, Y., Wang, P., Wang, Q., Zhou, Q., et al. (2022). Structure of the cytoplasmic ring of the Xenopus laevis nuclear pore complex. Science *376*, eabl8280. https://doi.org/10.1126/science.abl8280.
17. Fontana, P., Dong, Y., Pi, X., Tong, A.B., Hecksel, C.W., Wang, L., Fu, T.M., Bustamante, C., and Wu, H. (2022). Structure of cytoplasmic ring of nuclear pore complex by integrative cryo-EM and AlphaFold. Science *376*, eabm9326. https://doi.org/10.1126/science.abm9326.
18. Bui, K.H., von Appen, A., DiGuilio, A.L., Ori, A., Sparks, L., Mackmull, M.-T., Bock, T., Hagen, W., Andrés-Pons, A., Glavy, J.S., et al. (2013). Integrated Structural Analysis of the Human Nuclear Pore Complex Scaffold. Cell *155*, 1233–1243. https://doi.org/10.1016/j.cell.2013.10.055.
19. Lutzmann, M., Kunze, R., Buerer, A., Aebi, U., and Hurt, E. (2002). Modular self-assembly of a Y-shaped multiprotein complex from seven nucleoporins. EMBO J. *21*, 387–397. https://doi.org/10.1093/emboj/21.3.387.
20. Siniossoglou, S., Lutzmann, M., Santos-Rosa, H., Leonard, K., Mueller, S., Aebi, U., and Hurt, E. (2000). Structure and Assembly of the Nup84p Complex. J. Cell Biol. *149*, 41–54. https://doi.org/10.1083/jcb.149.1.41.
21. Fischer, J., Teimer, R., Amlacher, S., Kunze, R., and Hurt, E. (2015). Linker Nups connect the nuclear pore complex inner ring with the outer ring and transport channel. Nat. Struct. Mol. Biol. *22*, 774–781. https://doi.org/10.1038/nsmb.3084.
22. Stuwe, T., Bley, C.J., Thierbach, K., Petrovic, S., Schilbach, S., Mayo, D.J., Perriches, T., Rundlet, E.J., Jeon, Y.E., Collins, L.N., et al. (2015).

Architecture of the fungal nuclear pore inner ring complex. Science *350*, 56–64. https://doi.org/10.1126/science.aac9176.

23. Chug, H., Trakhanov, S., Hülsmann, B.B., Pleiner, T., and Görlich, D. (2015). Crystal structure of the metazoan Nup62•Nup58•Nup54 nucleoporin complex. Science *350*, 106–110. https://doi.org/10.1126/science.aac7420.

24. Upla, P., Kim, S.J., Sampathkumar, P., Dutta, K., Cahill, S.M., Chemmama, I.E., Williams, R., Bonanno, J.B., Rice, W.J., Stokes, D.L., et al. (2017). Molecular Architecture of the Major Membrane Ring Component of the Nuclear Pore Complex. Structure *25*, 434–445. https://doi.org/10.1016/j.str.2017.01.006.

25. Zhang, Y., Li, S., Zeng, C., Huang, G., Zhu, X., Wang, Q., Wang, K., Zhou, Q., Yan, C., Zhang, W., et al. (2020). Molecular architecture of the luminal ring of the Xenopus laevis nuclear pore complex. Cell Res. *30*, 532–540. https://doi.org/10.1038/s41422-020-0320-y.

26. Zimmerli, C.E., Allegretti, M., Rantos, V., Goetz, S.K., Obarska-Kosinska, A., Zagoriy, I., Halavatyi, A., Hummer, G., Mahamid, J., Kosinski, J., et al. (2021). Nuclear pores dilate and constrict in cellulo. Science *374*, eabd9776. https://doi.org/10.1126/science.abd9776.

27. Schuller, A.P., Wojtynek, M., Mankus, D., Tatli, M., Kronenberg-Tenga, R., Regmi, S.G., Dip, P.V., Lytton-Jean, A.K.R., Brignole, E.J., Dasso, M., et al. (2021). The cellular environment shapes the nuclear pore complex architecture. Nature *598*, 667–671. https://doi.org/10.1038/s41586-021-03985-3.

28. Zila, V., Margiotta, E., Turoňová, B., Müller, T.G., Zimmerli, C.E., Mattei, S., Allegretti, M., Börner, K., Rada, J., Müller, B., et al. (2021). Cone-shaped HIV-1 capsids are transported through intact nuclear pores. Cell *184*, 1032–1046.e18. https://doi.org/10.1016/j.cell.2021.01.025.

29. Mahamid, J., Pfeffer, S., Schaffer, M., Villa, E., Danev, R., Cuellar, L.K., Förster, F., Hyman, A.A., Plitzko, J.M., and Baumeister, W. (2016). Visualizing the molecular sociology at the HeLa cell nuclear periphery. Science *351*, 969–972. https://doi.org/10.1126/science.aad8857.

30. Andreu, I., Granero-Moya, I., Chahare, N.R., Clein, K., Molina-Jordán, M., Beedle, A.E.M., Elosegui-Artola, A., Abenza, J.F., Rossetti, L., Trepat, X., et al. (2022). Mechanical force application to the nucleus regulates nucleocytoplasmic transport. Nat. Cell Biol. *24*, 896–905. https://doi.org/10.1038/s41556-022-00927-7.

31. Bonner, J.T., and Shaw, M.J. (1957). The role of humidity in the differentiation of the cellular slime molds. J. Cell. Comp. Physiol. *50*, 145–153. https://doi.org/10.1002/jcp.1030500111.

32. Bonner, J.T., Davidowski, T.A., Hsu, W.-L., Lapeyrolerie, D.A., and Suthers, H.L.B. (1982). The Role of Surface Water and Light on Differentiation in the Cellular Slime Molds. Differentiation *21*, 123–126. https://doi.org/10.1111/j.1432-0436.1982.tb01204.x.

33. Hoffmann, E.K., Lambert, I.H., and Pedersen, S.F. (2009). Physiology of Cell Volume Regulation in Vertebrates. Physiol. Rev. *89*, 193–277. https://doi.org/10.1152/physrev.00037.2007.

34. Armstrong, C.M. (2003). The Na/K pump, Cl ion, and osmotic stabilization of cells. Proc. Natl. Acad. Sci. USA *100*, 6257–6262. https://doi.org/10.1073/pnas.0931278100.

35. Allen, R.D., and Naitoh, Y. (2002). Osmoregulation and contractile vacuoles of protozoa. Int. Rev. Cytol. *215*, 351–394. https://doi.org/10.1016/S0074-7696(02)15015-7.

36. Allen, R.D. (2000). The contractile vacuole and its membrane dynamics. BioEssays *22*, 1035–1042. https://doi.org/10.1002/1521-1878(200011)22:11<1035::AID-BIES10>3.0.CO;2-A.

37. Sun, B., Ma, H., and Firtel, R.A. (2003). Dictyostelium Stress-activated Protein Kinase α, a Novel Stress-activated Mitogen-activated Protein Kinase Kinase Kinase-like Kinase, Is Important for the Proper Regulation of the Cytoskeleton. Mol. Biol. Cell *14*, 4526–4540. https://doi.org/10.1091/mbc.E03-01-0039.

38. Araki, T., and Williams, J.G. (2012). Perturbations of the actin cytoskeleton activate a Dictyostelium STAT signalling pathway. Eur. J. Cell Biol. *91*, 420–425. https://doi.org/10.1016/j.ejcb.2012.01.002.

39. Ott, A., Oehme, F., Keller, H., and Schuster, S.C. (2000). Osmotic stress response in Dictyostelium is mediated by cAMP. EMBO J. *19*, 5782–5792. https://doi.org/10.1093/emboj/19.21.5782.

40. Pintsch, T., Satre, M., Klein, G., Martin, J.B., and Schuster, S.C. (2001). Cytosolic acidification as a signal mediating hyperosmotic stress responses in Dictyostelium discoideum. BMC Cell Biol. *2*, 9. https://doi.org/10.1186/1471-2121-2-9.

41. Zischka, H., Oehme, F., Pintsch, T., Ott, A., Keller, H., Kellermann, J., and Schuster, S.C. (1999). Rearrangement of cortex proteins constitutes an osmoprotective mechanism in Dictyostelium. EMBO J. *18*, 4241–4249. https://doi.org/10.1093/emboj/18.15.4241.

42. Lang, F., Busch, G.L., Ritter, M., Völkl, H., Waldegger, S., Gulbins, E., and Häussinger, D. (1998). Functional Significance of Cell Volume Regulatory Mechanisms. Physiol. Rev. *78*, 247–306. https://doi.org/10.1152/physrev.1998.78.1.247.

43. Kitamura, A., Oasa, S., Kawaguchi, H., Osaka, M., Vukojević, V., and Kinjo, M. (2023). Increased intracellular crowding during hyperosmotic stress. Sci. Rep. *13*, 11834. https://doi.org/10.1038/s41598-023-39090-w.

44. Watanabe, K., Morishita, K., Zhou, X., Shiizaki, S., Uchiyama, Y., Koike, M., Naguro, I., and Ichijo, H. (2021). Cells recognize osmotic stress through liquid–liquid phase separation lubricated with poly(ADP-ribose). Nat. Commun. *12*, 1353. https://doi.org/10.1038/s41467-021-21614-5.

45. Cantwell, H., and Nurse, P. (2019). Unravelling nuclear size control. Curr. Genet. *65*, 1281–1285. https://doi.org/10.1007/s00294-019-00999-3.

46. Deviri, D., and Safran, S.A. (2022). Balance of osmotic pressures determines the nuclear-to-cytoplasmic volume ratio of the cell. Proc. Natl. Acad. Sci. USA *119*, e2118301119. https://doi.org/10.1073/pnas.2118301119.

47. Lemière, J., Real-Calderon, P., Holt, L.J., Fai, T.G., and Chang, F. (2022). Control of nuclear size by osmotic forces in Schizosaccharomyces pombe. eLife *11*, e76075. https://doi.org/10.7554/eLife.76075.

48. Mazzanti, M., Bustamante, J.O., and Oberleithner, H. (2001). Electrical Dimension of the Nuclear Envelope. Physiol. Rev. *81*, 1–19. https://doi.org/10.1152/physrev.2001.81.1.1.

49. Matzke, A.J.M., Weiger, T.M., and Matzke, M. (2010). Ion channels at the nucleus: Electrophysiology meets the genome. Mol. Plant *3*, 642–652. https://doi.org/10.1093/mp/ssq013.

50. Hoffmann, P.C., Kreysing, J.P., Khusainov, I., Tuijtel, M.W., Welsch, S., and Beck, M. (2022). Structures of the eukaryotic ribosome and its translational states in situ. Nat. Commun. *13*, 7435. https://doi.org/10.1038/s41467-022-34997-w.

51. Cruz-León, S., Majtner, T., Hoffmann, P.C., Kreysing, J.P., Kehl, S., Tuijtel, M.W., Schaefer, S.L., Geißler, K., Beck, M., Turoňová, B., et al. (2024). High-confidence 3D template matching for cryo-electron tomography. Nat. Commun. *15*, 3992. https://doi.org/10.1038/s41467-024-47839-8.

52. Xing, H., Taniguchi, R., Khusainov, I., Kreysing, J.P., Welsch, S., Turoňová, B., and Beck, M. (2023). Translation dynamics in human cells visualized at high resolution reveal cancer drug action. Science *381*, 70–75. https://doi.org/10.1126/science.adh1411.

53. Xue, L., Lenz, S., Zimmermann-Kogadeeva, M., Tegunov, D., Cramer, P., Bork, P., Rappsilber, J., and Mahamid, J. (2022). Visualizing translation dynamics at atomic detail inside a bacterial cell. Nature *610*, 205–211. https://doi.org/10.1038/s41586-022-05255-2.

54. Khusainov, I., Romanov, N., Goemans, C., Turoňová, B., Zimmerli, C.E., Welsch, S., Langer, J.D., Typas, A., and Beck, M. (2024). Bactericidal effect of tetracycline in E. coli strain ED1a may be associated with ribosome dysfunction. Nat. Commun. *15*, 4783. https://doi.org/10.1038/s41467-024-49084-5.

55. Tan, Z.Y., Cai, S., Noble, A.J., Chen, J.K., Shi, J., and Gan, L. (2023). Heterogeneous non-canonical nucleosomes predominate in yeast cells in situ. eLife *12*, RP87672. https://doi.org/10.7554/eLife.87672.

56. Jumper, J., Evans, R., Pritzel, A., Green, T., Figurnov, M., Ronneberger, O., Tunyasuvunakool, K., Bates, R., Žídek, A., Potapenko, A., et al. (2021). Highly accurate protein structure prediction with AlphaFold. Nature *596*, 583–589. https://doi.org/10.1038/s41586-021-03819-2.

57. Evans, R., O'Neill, M., Pritzel, A., Antropova, N., Senior, A., Green, T., Žídek, A., Bates, R., Blackwell, S., Yim, J., et al. (2022). Protein complex prediction with AlphaFold-Multimer. Preprint at bioRxiv. https://doi.org/10.1101/2021.10.04.463034.

58. van Kempen, M., Kim, S.S., Tumescheit, C., Mirdita, M., Lee, J., Gilchrist, C.L.M., Söding, J., and Steinegger, M. (2024). Fast and accurate protein structure search with Foldseek. Nat. Biotechnol. *42*, 243–246. https://doi.org/10.1038/s41587-023-01773-0.

59. Mosalaganti, S., Kosinski, J., Albert, S., Schaffer, M., Strenkert, D., Salomé, P.A., Merchant, S.S., Plitzko, J.M., Baumeister, W., Engel, B.D., et al. (2018). In situ architecture of the algal nuclear pore complex. Nat. Commun. *9*, 2361. https://doi.org/10.1038/s41467-018-04739-y.

60. Allegretti, M., Zimmerli, C.E., Rantos, V., Wilfling, F., Ronchi, P., Fung, H.K.H., Lee, C.W., Hagen, W., Turoňová, B., Karius, K., et al. (2020). In-cell architecture of the nuclear pore and snapshots of its turnover. Nature *586*, 796–800. https://doi.org/10.1038/s41586-020-2670-5.

61. Bilokapic, S., and Schwartz, T.U. (2012). Molecular basis for Nup37 and ELY5/ELYS recruitment to the nuclear pore complex. Proc. Natl. Acad. Sci. USA *109*, 15241–15246. https://doi.org/10.1073/pnas.1205151109.

62. Winey, M., Yarar, D., Giddings, T.H., and Mastronarde, D.N. (1997). Nuclear Pore Complex Number and Distribution throughout the Saccharomyces cerevisiae Cell Cycle by Three-Dimensional Reconstruction from Electron Micrographs of Nuclear Envelopes. Mol. Biol. Cell *8*, 2119–2132. https://doi.org/10.1091/mbc.8.11.2119.

63. Peters, R. (1984). Nucleo-cytoplasmic flux and intracellular mobility in single hepatocytes measured by fluorescence microphotolysis. EMBO J. *3*, 1831–1836. https://doi.org/10.1002/j.1460-2075.1984.tb02055.x.

64. Beck, M., Schmidt, A., Malmstroem, J., Claassen, M., Ori, A., Szymborska, A., Herzog, F., Rinner, O., Ellenberg, J., and Aebersold, R. (2011). The quantitative proteome of a human cell line. Mol. Syst. Biol. *7*, 549. https://doi.org/10.1038/msb.2011.82.

65. Dick, D.A.T. (1964). The Permeability Coefficient of Water in the Cell Membrane and the Diffusion Coefficient in the Cell Interior. J. Theor. Biol. *7*, 504–531. https://doi.org/10.1016/0022-5193(64)90019-0.

66. Olbrich, K., Rawicz, W., Needham, D., and Evans, E. (2000). Water permeability and mechanical strength of polyunsaturated lipid bilayers. Biophys. J. *79*, 321–327. https://doi.org/10.1016/S0006-3495(00)76294-1.

67. van Meer, G., Voelker, D.R., and Feigenson, G.W. (2008). Membrane lipids: where they are and how they behave. Nat. Rev. Mol. Cell Biol. *9*, 112–124. https://doi.org/10.1038/nrm2330.

68. Le Gall, S., Neuhof, A., and Rapoport, T. (2004). The Endoplasmic Reticulum Membrane Is Permeable to Small Molecules. Mol. Biol. Cell *15*, 447–455. https://doi.org/10.1091/mbc.E03-05-0325.

69. Antonny, B., Vanni, S., Shindou, H., and Ferreira, T. (2015). From zero to six double bonds: Phospholipid unsaturation and organelle function. Trends Cell Biol. *25*, 427–436. https://doi.org/10.1016/j.tcb.2015.03.004.

70. Finkelstein, A., and Cass, A. (1967). Effect of Cholesterol on the Water Permeability of Thin Lipid Membranes. Nature *216*, 717–718. https://doi.org/10.1038/216717a0.

71. von Bülow, S., Siggel, M., Linke, M., and Hummer, G. (2019). Dynamic cluster formation determines viscosity and diffusion in dense protein solutions. Proc. Natl. Acad. Sci. USA *116*, 9843–9852. https://doi.org/10.1073/pnas.1817564116.

72. Zimmerman, S.B., and Trach, S.O. (1991). Estimation of Macromolecule Concentrations and Excluded Volume Effects for the Cytoplasm of Escherichia coli. J. Mol. Biol. *222*, 599–620. https://doi.org/10.1016/0022-2836(91)90499-v.

73. Nishiyama, N., and Yokoyama, T. (2017). Permeability of porous media: role of the critical pore size. J. Geophys. Res. Solid Earth *122*, 6955–6971. https://doi.org/10.1002/2016JB013793.

74. Walsh, J.B., and Brace, W.F. (1984). The effect of pressure on porosity and the transport properties of rock. J. Geophys. Res. *89*, 9425–9431. https://doi.org/10.1029/JB089iB11p09425.

75. Gueguen, Y., and Dienes, J. (1989). Transport Properties of Rocks from Statistics and Percolation. Math. Geol. *21*, 1–13. https://doi.org/10.1007/BF00897237.

76. Sarout, J. (2012). Impact of pore space topology on permeability, cut-off frequencies and validity of wave propagation theories. Geophys. J. Int. *189*, 481–492. https://doi.org/10.1111/j.1365-246X.2011.05329.x.

77. Costa, A. (2006). Permeability-porosity relationship: A reexamination of the Kozeny-Carman equation based on a fractal pore-space geometry assumption. Geophys. Res. Lett. *33*, L02318. https://doi.org/10.1029/2005GL025134.

78. Frey, S., Richter, R.P., and Görlich, D. (2006). FG-rich repeats of nuclear pore proteins form a three-dimensional meshwork with hydrogel-like properties. Science *314*, 815–817. https://doi.org/10.1126/science.1132516.

79. Frey, S., and Görlich, D. (2007). A Saturated FG-Repeat Hydrogel Can Reproduce the Permeability Properties of Nuclear Pore Complexes. Cell *130*, 512–523. https://doi.org/10.1016/j.cell.2007.06.024.

80. Schmidt, H.B., and Görlich, D. (2015). Nup98 FG domains from diverse species spontaneously phase-separate into particles with nuclear pore-like permselectivity. eLife *4*, e04251. https://doi.org/10.7554/eLife.04251.

81. Deviri, D., Pfeifer, C.R., Dooling, L.J., Ivanovska, I.L., Discher, D.E., and Safran, S.A. (2019). Scaling laws indicate distinct nucleation mechanisms of holes in the nuclear lamina. Nat. Phys. *15*, 823–829. https://doi.org/10.1038/s41567-019-0506-8.

82. Miyamoto, Y., Itoh, Y., Suzuki, T., Tanaka, T., Sakai, Y., Koido, M., Hata, C., Wang, C.X., Otani, M., Moriishi, K., et al. (2022). SARS-CoV-2 ORF6 disrupts nucleocytoplasmic trafficking to advance viral replication. Commun. Biol. *5*, 483. https://doi.org/10.1038/s42003-022-03427-4.

83. Kato, K., Ikliptikawati, D.K., Kobayashi, A., Kondo, H., Lim, K., Hazawa, M., and Wong, R.W. (2021). Overexpression of SARS-CoV-2 protein ORF6 dislocates RAE1 and NUP98 from the nuclear pore complex. Biochem. Biophys. Res. Commun. *536*, 59–66. https://doi.org/10.1016/j.bbrc.2020.11.115.

84. Makio, T., Zhang, K., Love, N., Mast, F.D., Liu, X., Elaish, M., Hobman, T., Aitchison, J.D., Fontoura, B.M.A., and Wozniak, R.W. (2024). SARS-CoV-2 Orf6 is positioned in the nuclear pore complex by Rae1 to inhibit nucleocytoplasmic transport. Mol. Biol. Cell *35*, ar62. https://doi.org/10.1091/mbc.E23-10-0386.

85. Taniguchi, R., Orniacki, C., Philipp Kreysing, J., Zila, V., Böhm, S., Turoňová, B., Kräusslich, H.-G., Doye, V., and Beck, M. (2024). Nuclear pores safeguard the integrity of the nuclear envelope. Preprint at bioRxiv. https://doi.org/10.1101/2024.02.05.578890.

86. Philipp Kreysing, J., Heidari, M., Zila, V., Cruz-Leon, S., Obarska-Kosinska, A., Laketa, V., Welsch, S., Köfinger, J., Hummer, G., Kräusslich, H.-G., et al. (2024). Passage of the HIV capsid cracks the nuclear pore. Preprint at bioRxiv. https://doi.org/10.1101/2024.04.23.590733.

87. Makarov, A.A., Padilla-Mejia, N.E., and Field, M.C. (2021). Evolution and diversification of the nuclear pore complex. Biochem. Soc. Trans. *49*, 1601–1619. https://doi.org/10.1042/BST20200570.

88. Komeili, A., and O'Shea, E.K. (2001). New perspectives on nuclear transport. Annu. Rev. Genet. *35*, 341–364. https://doi.org/10.1146/annurev.genet.35.102401.090720.

89. Ribbeck, K., and Görlich, D. (2001). Kinetic analysis of translocation through nuclear pore complexes. EMBO J. *20*, 1320–1330. https://doi.org/10.1093/emboj/20.6.1320.

90. Karlsson, T., Glogauer, M., Ellen, R.P., Loitto, V.-M., Magnusson, K.-E., and Magalhães, M.A.O. (2011). Aquaporin 9 phosphorylation mediates membrane localization and neutrophil polarization. J. Leukoc. Biol. *90*, 963–973. https://doi.org/10.1189/jlb.0910540.

91. Frallicciardi, J., Melcr, J., Siginou, P., Marrink, S.J., and Poolman, B. (2022). Membrane thickness, lipid phase and sterol type are determining factors in the permeability of membranes to small solutes. Nat. Commun. *13*, 1605. https://doi.org/10.1038/s41467-022-29272-x.

92. Lim, R.Y.H., Fahrenkrog, B., Köser, J., Schwarz-Herion, K., Deng, J., and Aebi, U. (2007). Nanomechanical Basis of Selective Gating by the Nuclear Pore Complex. Science *318*, 640–643. https://doi.org/10.1126/science.1145980.

93. Ma, J., Goryaynov, A., Sarma, A., and Yang, W. (2012). Self-regulated viscous channel in the nuclear pore complex. Proc. Natl. Acad. Sci. USA *109*, 7326–7331. https://doi.org/10.1073/pnas.1201724109.

94. Klughammer, N., Barth, A., Dekker, M., Onck, P.R., and Dekker, C. (2024). Diameter Dependence of Transport through Nuclear Pore Complex Mimics Studied Using Optical Nanopores. eLife *12*, RP87174. https://doi.org/10.1101/2023.02.18.529008.

95. McCloskey, A., Ibarra, A., and Hetzer, M.W. (2018). Tpr regulates the total number of nuclear pore complexes per cell nucleus. Genes Dev. *32*, 1321–1331. https://doi.org/10.1101/GAD.315523.118.

96. Thaller, D.J., and Patrick Lusk, C. (2018). Fantastic nuclear envelope herniations and where to find them. Biochem. Soc. Trans. *46*, 877–889. https://doi.org/10.1042/BST20170442.

97. Jevtić, P., Schibler, A.C., Wesley, C.C., Pegoraro, G., Misteli, T., and Levy, D.L. (2019). The nucleoporin ELYS regulates nuclear size by controlling NPC number and nuclear import capacity. EMBO Rep. *20*, e47283. https://doi.org/10.15252/embr.201847283.

98. Nava, M.M., Miroshnikova, Y.A., Biggs, L.C., Whitefield, D.B., Metge, F., Boucas, J., Vihinen, H., Jokitalo, E., Li, X., García Arcos, J.M., et al. (2020). Heterochromatin-Driven Nuclear Softening Protects the Genome against Mechanical Stress-Induced Damage. Cell *181*, 800–817.e22. https://doi.org/10.1016/j.cell.2020.03.052.

99. Raab, M., Gentili, M., De Belly, H., Thiam, H.R., Vargas, P., Jimenez, A.J., Lautenschlaeger, F., Voituriez, R., Lennon-Duménil, A.M., Manel, N., et al. (2016). ESCRT III repairs nuclear envelope ruptures during cell migration to limit DNA damage and cell death. Science *352*, 359–362. https://doi.org/10.1126/science.aad7611.

100. Denais, C.M., Gilbert, R.M., Isermann, P., McGregor, A.L., te Lindert, M., Weigelin, B., Davidson, P.M., Friedl, P., Wolf, K., and Lammerding, J. (2016). Nuclear envelope rupture and repair during cancer cell migration. Science *352*, 353–358. https://doi.org/10.1126/science.aad7297.

101. Liu, Y.J., Le Berre, M., Lautenschlaeger, F., Maiuri, P., Callan-Jones, A., Heuzé, M., Takaki, T., Voituriez, R., and Piel, M. (2015). Confinement and low adhesion induce fast amoeboid migration of slow mesenchymal cells. Cell *160*, 659–672. https://doi.org/10.1016/j.cell.2015.01.007.

102. Beck, M. (2006). Strukturelle Analyse von Kernporenkomplexen mittels Kryoelektronentomographie. PhD thesis (Max-Planck-Institut für Biochemie Abteilung für Molekulare Strukturbiologie). https://nbn-resolving.de/urn/resolver.pl?urn:nbn:de:bvb:91-diss20060126-0938494509.

103. Paschke, P., Knecht, D.A., Silale, A., Traynor, D., Williams, T.D., Thomason, P.A., Insall, R.H., Chubb, J.R., Kay, R.R., and Veltman, D.M. (2018). Rapid and efficient genetic engineering of both wild type and axenic strains of Dictyostelium discoideum. PLoS One *13*, e0196809. https://doi.org/10.1371/journal.pone.0196809.

104. Gordon, D.E., Jang, G.M., Bouhaddou, M., Xu, J., Obernier, K., White, K.M., O'Meara, M.J., Rezelj, V.V., Guo, J.Z., Swaney, D.L., et al. (2020). A SARS-CoV-2 protein interaction map reveals targets for drug repurposing. Nature *583*, 459–468. https://doi.org/10.1038/s41586-020-2286-9.

105. Schindelin, J., Arganda-Carreras, I., Frise, E., Kaynig, V., Longair, M., Pietzsch, T., Preibisch, S., Rueden, C., Saalfeld, S., Schmid, B., et al. (2012). Fiji: an open-source platform for biological-image analysis. Nat. Methods *9*, 676–682. https://doi.org/10.1038/nmeth.2019.

106. Ollion, J., Cochennec, J., Loll, F., Escudé, C., and Boudier, T. (2013). TANGO: A generic tool for high-throughput 3D image analysis for studying nuclear organization. Bioinformatics *29*, 1840–1841. https://doi.org/10.1093/bioinformatics/btt276.

107. Klumpe, S., Fung, H.K.H., Goetz, S.K., Zagoriy, I., Hampoelz, B., Zhang, X., Erdmann, P.S., Baumbach, J., Müller, C.W., Beck, M., et al. (2021). A Modular Platform for Automated Cryo-FIB Workflows. eLife *10*, e70506. https://doi.org/10.7554/eLife.70506.

108. Mastronarde, D.N. (2005). Automated electron microscope tomography using robust prediction of specimen movements. J. Struct. Biol. *152*, 36–51. https://doi.org/10.1016/j.jsb.2005.07.007.

109. Kremer, J.R., Mastronarde, D.N., and McIntosh, J.R. (1996). Computer visualization of three-dimensional image data using IMOD. J. Struct. Biol. *116*, 71–76. https://doi.org/10.1006/jsbi.1996.0013.

110. Turoňová, B., Schur, F.K.M., Wan, W., and Briggs, J.A.G. (2017). Efficient 3D-CTF correction for cryo-electron tomography using NovaCTF improves subtomogram averaging resolution to 3.4Å. J. Struct. Biol. *199*, 187–195. https://doi.org/10.1016/j.jsb.2017.07.007.

111. Tegunov, D., and Cramer, P. (2019). Real-time cryo-electron microscopy data preprocessing with Warp. Nat. Methods *16*, 1146–1152. https://doi.org/10.1038/s41592-019-0580-y.

112. Zivanov, J., Nakane, T., Forsberg, B.O., Kimanius, D., Hagen, W.J., Lindahl, E., and Scheres, S.H. (2018). New tools for automated high-resolution cryo-EM structure determination in RELION-3. eLife *7*, 163. https://doi.org/10.7554/eLife.42166.

113. Tegunov, D., Xue, L., Dienemann, C., Cramer, P., and Mahamid, J. (2021). Multi-particle cryo-EM refinement with M visualizes ribosome-antibiotic complex at 3.5 Å in cells. Nat. Methods *18*, 186–193. https://doi.org/10.1038/s41592-020-01054-7.

114. Turoňová, B., Sikora, M., Schürmann, C., Hagen, W.J.H., Welsch, S., Blanc, F.E.C., von Bülow, S., Gecht, M., Bagola, K., Hörner, C., et al. (2020). In situ structural analysis of SARS-CoV-2 spike reveals flexibility mediated by three hinges. Science *370*, 203–208. https://doi.org/10.1126/science.abd5223.

115. Wan, W., Khavnekar, S., Wagner, J., Erdmann, P., and Baumeister, W. (2020). STOPGAP: A Software Package for Subtomogram Averaging and Refinement. Microsc. Microanal. *26*, 2516. https://doi.org/10.1017/S143192762002187X.

116. Wan, W., Khavnekar, S., and Wagner, J. (2024). STOPGAP, an open-source package for template matching, subtomogram alignment, and classification. Acta Crystallogr. D Struct. Biol. *80*, 336–349. https://doi.org/10.1107/S205979832400295X.

117. Burt, A., Gaifas, L., Dendooven, T., and Gutsche, I. (2021). A flexible framework for multi-particle refinement in cryo-electron tomography. PLoS Biol. *19*, e3001319.. https://doi.org/10.1371/journal.pbio.3001319.

118. Ermel, U.H., Arghittu, S.M., and Frangakis, A.S. (2022). ArtiaX: An electron tomography toolbox for the interactive handling of sub-tomograms in UCSF ChimeraX. Protein Sci. *31*, e4472. https://doi.org/10.1002/pro.4472.

119. Pettersen, E.F., Goddard, T.D., Huang, C.C., Couch, G.S., Greenblatt, D.M., Meng, E.C., and Ferrin, T.E. (2004). UCSF Chimera–a visualization system for exploratory research and analysis. J. Comput. Chem. *25*, 1605–1612. https://doi.org/10.1002/jcc.20084.

120. Goddard, T.D., Huang, C.C., Meng, E.C., Pettersen, E.F., Couch, G.S., Morris, J.H., and Ferrin, T.E. (2018). UCSF ChimeraX: Meeting modern challenges in visualization and analysis. Protein Sci. *27*, 14–25. https://doi.org/10.1002/pro.3235.

121. Katoh, K., Misawa, K., Kuma, K.-I., and Miyata, T. (2002). MAFFT: a novel method for rapid multiple sequence alignment based on fast Fourier transform. Nucleic Acids Res. *30*, 3059–3066. https://doi.org/10.1093/nar/gkf436.

122. Finn, R.D., Clements, J., and Eddy, S.R. (2011). HMMER web server: Interactive sequence similarity searching. Nucleic Acids Res. *39*, W29–W37. https://doi.org/10.1093/nar/gkr367.

123. Yu, D., Chojnowski, G., Rosenthal, M., and Kosinski, J. (2023). AlphaPulldown-a python package for protein-protein interaction screens using AlphaFold-Multimer. Bioinformatics *39*, btac749. https://doi.org/10.1093/bioinformatics/btac749.

124. Mirdita, M., Schütze, K., Moriwaki, Y., Heo, L., Ovchinnikov, S., and Steinegger, M. (2022). ColabFold: making protein folding accessible to all. Nat. Methods *19*, 679–682. https://doi.org/10.1038/s41592-022-01488-1.

125. Rantos, V., Karius, K., and Kosinski, J. (2022). Integrative structural modeling of macromolecular complexes using Assembline. Nat. Protoc. *17*, 152–176. https://doi.org/10.1038/s41596-021-00640-z.

126. Strimmer, K. (2008). fdrtool: A versatile R package for estimating local and tail area-based false discovery rates. Bioinformatics *24*, 1461–1462. https://doi.org/10.1093/bioinformatics/btn209.

127. Webb, B., Viswanath, S., Bonomi, M., Pellarin, R., Greenberg, C.H., Saltzberg, D., and Sali, A. (2018). Integrative structure modeling with the Integrative Modeling Platform. Protein Sci. *27*, 245–258. https://doi.org/10.1002/pro.3311.

128. Saltzberg, D., Greenberg, C.H., Viswanath, S., Chemmama, I., Webb, B., Pellarin, R., Echeverria, I., and Sali, A. (2019). Modeling Biological Complexes Using Integrative Modeling Platform. Biomolecular Simulations. Methods Protoc. 353–377. https://doi.org/10.1007/978-1-4939-9608-7_15.

129. Abraham, M.J., Murtola, T., Schulz, R., Páll, S., Smith, J.C., Hess, B., and Lindahl, E. (2015). Gromacs: High performance molecular simulations through multi-level parallelism from laptops to supercomputers. SoftwareX *1–2*, 19–25. https://doi.org/10.1016/j.softx.2015.06.001.

130. Malhotra, S., Joseph, A.P., Thiyagalingam, J., and Topf, M. (2021). Assessment of protein–protein interfaces in cryo-EM derived assemblies. Nat. Commun. *12*, 3399. https://doi.org/10.1038/s41467-021-23692-x.

131. Winn, M.D., Ballard, C.C., Cowtan, K.D., Dodson, E.J., Emsley, P., Evans, P.R., Keegan, R.M., Krissinel, E.B., Leslie, A.G.W., McCoy, A., et al. (2011). Overview of the CCP4 suite and current developments. Acta Crystallogr. D Biol. Crystallogr. *67*, 235–242. https://doi.org/10.1107/S0907444910045749.

132. Pupko, T., Bell, R.E., Mayrose, I., Glaser, F., and Ben-Tal, N. (2002). Rate4Site: an algorithmic tool for the identification of functional regions in proteins by surface mapping of evolutionary determinants within their homologues. Bioinformatics *18*, S71–S77. https://doi.org/10.1093/bioinformatics/18.suppl_1.S71.

133. Krissinel, E., and Henrick, K. (2007). Inference of Macromolecular Assemblies from Crystalline State. J. Mol. Biol. *372*, 774–797. https://doi.org/10.1016/j.jmb.2007.05.022.

134. Müller-Taubenberger, A. (2006). Application of Fluorescent Protein Tags as Reporters in Live-Cell Imaging Studies. Methods Mol. Biol. *346*, 229–246. https://doi.org/10.1385/1-59745-144-4:229.

135. Hagen, W.J.H., Wan, W., and Briggs, J.A.G. (2017). Implementation of a cryo-electron tomography tilt-scheme optimized for high resolution subtomogram averaging. J. Struct. Biol. *197*, 191–198. https://doi.org/10.1016/j.jsb.2016.06.007.

136. Grant, T., and Grigorieff, N. (2015). Measuring the optimal exposure for single particle cryo-EM using a 2.6 Å reconstruction of rotavirus. eLife *4*, e06980. https://doi.org/10.7554/eLife.06980.001.

137. Wan, W., Kolesnikova, L., Clarke, M., Koehler, A., Noda, T., Becker, S., and Briggs, J.A.G. (2017). Structure and assembly of the Ebola virus nucleocapsid. Nature *551*, 394–397. https://doi.org/10.1038/nature24490.

138. Shao, S., Murray, J., Brown, A., Taunton, J., Ramakrishnan, V., and Hegde, R.S. (2016). Decoding Mammalian Ribosome-mRNA States by Translational GTPase Complexes. Cell *167*, 1229–1240.e15. https://doi.org/10.1016/j.cell.2016.10.046.

139. Smith, P.R., Loerch, S., Kunder, N., Stanowick, A.D., Lou, T.-F., and Campbell, Z.T. (2021). Functionally distinct roles for eEF2K in the control of ribosome availability and p-body abundance. Nat. Commun. *12*, 6789. https://doi.org/10.1038/s41467-021-27160-4.

140. Buschauer, R., Matsuo, Y., Sugiyama, T., Chen, Y.-H., Alhusaini, N., Sweet, T., Ikeuchi, K., Cheng, J., Matsuki, Y., Nobuta, R., et al. (2020). The Ccr4-Not complex monitors the translating ribosome for codon optimality. Science *368*, eaay6912. https://doi.org/10.1126/science.aay6912.

141. Yamamoto, H., Unbehaun, A., Loerke, J., Behrmann, E., Collier, M., Bürger, J., Mielke, T., and Spahn, C.M.T. (2014). Structure of the mammalian 80S initiation complex with initiation factor 5B on HCV-IRES RNA. Nat. Struct. Mol. Biol. *21*, 721–727. https://doi.org/10.1038/nsmb.2859.

142. Huerta-Cepas, J., Szklarczyk, D., Heller, D., Hernández-Plaza, A., Forslund, S.K., Cook, H., Mende, D.R., Letunic, I., Rattei, T., Jensen, L.J., et al. (2019). EggNOG 5.0: A hierarchical, functionally and phylogenetically annotated orthology resource based on 5090 organisms and 2502 viruses. Nucleic Acids Res. *47*, D309–D314. https://doi.org/10.1093/nar/gky1085.

143. Gabler, F., Nam, S.Z., Till, S., Mirdita, M., Steinegger, M., Söding, J., Lupas, A.N., and Alva, V. (2020). Protein Sequence Analysis Using the MPI Bioinformatics Toolkit. Curr. Protoc. Bioinformatics *72*, e108. https://doi.org/10.1002/cpbi.108.

144. Altschul, S.F., Gish, W., Miller, W., Myers, E.W., and Lipman, D.J. (1990). Basic local alignment search tool. J. Mol. Biol. *215*, 403–410. https://doi.org/10.1016/S0022-2836(05)80360-2.

145. Pruitt, K.D., Tatusova, T., and Maglott, D.R. (2005). NCBI Reference Sequence (RefSeq): A curated non-redundant sequence database of genomes, transcripts and proteins. Nucleic Acids Res. *33*, D501–D504. https://doi.org/10.1093/nar/gki025.

146. Zhang, Y., and Skolnick, J. (2005). TM-align: A protein structure alignment algorithm based on the TM-score. Nucleic Acids Res. *33*, 2302–2309. https://doi.org/10.1093/nar/gki524.

147. Tai, L., Zhu, Y., Ren, H., Huang, X., Zhang, C., and Sun, F. (2022). 8 Å structure of the outer rings of the Xenopus laevis nuclear pore complex obtained by cryo-EM and AI. Protein Cell *13*, 760–777. https://doi.org/10.1007/s13238-021-00895-y.

148. Von Appen, A., Kosinski, J., Sparks, L., Ori, A., DiGuilio, A.L., Vollmer, B., Mackmull, M.T., Banterle, N., Parca, L., Kastritis, P., et al. (2015). In situ structural analysis of the human nuclear pore complex. Nature *526*, 140–143. https://doi.org/10.1038/nature15381.

149. Kosinski, J., Mosalaganti, S., Von Appen, A., Teimer, R., Diguilio, A.L., Wan, W., Bui, K.H., Hagen, W.J.H., Briggs, J.A.G., Glavy, J.S., et al. (2016). Molecular architecture of the inner ring scaffold of the human nuclear pore complex. Science *352*, 363–365. https://doi.org/10.1126/science.aaf0643.

150. Benjamini, Y., and Hochberg, Y. (1995). Controlling the False Discovery Rate: A Practical and Powerful Approach to Multiple Testing. J. R. Stat. Soc. Series B Stat. Methodol. *57*, 289–300. https://doi.org/10.1111/j.2517-6161.1995.tb02031.x.

151. Heinrich, L., Bennett, D., Ackerman, D., Park, W., Bogovic, J., Eckstein, N., Petruncio, A., Clements, J., Pang, S., Xu, C.S., et al. (2021). Whole-cell organelle segmentation in volume electron microscopy. Nature *599*, 141–146. https://doi.org/10.1038/s41586-021-03977-3.

152. Jackson, D.A. (2011). The Cell Nucleus: Biogenesis, Structure, and Function. In Encyclopedia of Molecular Cell Biology and Molecular

Medicine (Wiley-VCH Verlag GmbH & Co. KGaA). https://doi.org/10.1002/3527600906.mcb.200300097.pub2.

153. Nagy, E., Hegedüs, I., Rehman, D., Wei, Q.J., Ahdab, Y.D., and Lienhard, J.H. (2021). The need for accurate osmotic pressure and mass transfer resistances in modeling osmotically driven membrane processes. Membranes (Basel) *11*, 1–34. https://doi.org/10.3390/membranes11020128.

154. Zheng, L., and Zheng, X. (2017). Numerical Methods. Chapter 8. In Modeling and Analysis of Modern Fluid Problems, L. Zheng and X. Zhang, eds. (Academic Press), pp. 361–455. https://doi.org/10.1016/B978-0-12-811753-8.22001-X.

155. Atangana, A. (2018). Principle of Groundwater Flow. Chapter 2. In Fractional Operators with Constant and Variable Order with Application to Geo-hydrology, A. Atangana, ed. (Academic Press), pp. 15–47. https://doi.org/10.1016/B978-0-12-809670-3.00002-3.

156. Darcy, H. (1856). Les fontaines publiques de la ville de Dijon: exposition et application des principes à suivre et des formules à employer dans les questions de distribution d'eau (V. Dalmont).

STAR★METHODS

KEY RESOURCES TABLE

REAGENT or RESOURCE	SOURCE	IDENTIFIER
Chemicals, peptides, and recombinant proteins		
Ampicillin	Sigma-Aldrich	A9518
G418	Sigma-Aldrich	G5013
Hygromycin B	Formedium	HYG5000
Hygromycin B	Thermo Fisher Scientific (Invitrogen)	10687010
HL5 medium w/o glucose	Formedium	HLB0102
FITC-dextran 500kDa mol wt	Sigma-Aldrich	FD500S
Digitonin	Sigma-Aldrich	D141
Hoechst-33342	Thermo Scientific	62249
Dulbecco's modified Eagle's medium	Sigma-Aldrich	D5796
Fetal Bovine Serum	Gibco	10270-106
Phosphate buffered saline	Sigma-Aldrich	D8537
Penicillin-Streptomycin, 10,000U/ml	Gibco	15140-122
Trypsin-EDTA (0.05%), phenol red	Gibco	25300-054
Lipofectamine 3000	Thermo Fisher Scientific (Invitrogen)	L3000001
Deposited data		
Cryo-tomogram *D. discoideum* - control condition (HL5), related to Figure 1B	This study	EMD-52053
Cryo-tomogram *D. discoideum* ~1 min hyper-OS (HL5+0.4M sorbitol), related to Figure 1B	This study	EMD-52054
Cryo-tomogram *D. discoideum* ~1 min hypo-OS (ddH2O), related to Figure 1B	This study	EMD-52055
Cryo-ET tilt series dataset of *D. discoideum* in HL5 medium (control condition)	This study	EMPIAR-11845
Cryo-ET tilt series dataset of *D. discoideum* in 0.4 M sorbitol (hyperosmotic stress)	This study	EMPIAR-11943
Cryo-ET tilt series dataset of *D. discoideum* in distilled H2O (hypoosmotic stress)	This study	EMPIAR-11944
Composite STA map of the *D. discoideum* nuclear pore complex in cells	This study	EMD-19137
Integrative structural model of the *D. discoideum* nuclear pore complex in cells	This study	PDB: 9HCJ
Asymmetric subunit STA map of the *D. discoideum* NPC	This study	EMD-19139
Focused map of the inner ring segment of the *D. discoideum* NPC	This study	EMD-19140
Focused map of the cytoplasmic ring segment of the *D. discoideum* NPC	This study	EMD-19141
Focused map of the nuclear ring segment of the *D. discoideum* NPC	This study	EMD-19142
Focused map of the lumenal ring segment of the *D. discoideum* NPC	This study	EMD-19143
Focused map around the basket connection of the *D. discoideum* NPC	This study	EMD-19144
Composite STA map of the *D. discoideum* NPC – control condition	This study	EMD-19149

(*Continued on next page*)

Continued

REAGENT or RESOURCE	SOURCE	IDENTIFIER
Asymmetric subunit STA map of the *D. discoideum* NPC – control condition	This study	EMD-19152
Composite STA map of the *D. discoideum* NPC – hyperosmotic stress	This study	EMD-19155
Asymmetric Subunit STA Map of the *D. discoideum* NPC – Hyperosmotic Stress	This study	EMD-19156
Composite STA map of the *D. discoideum* NPC – hypoosmotic stress	This study	EMD-19157
Asymmetric subunit STA map of the *D. discoideum* NPC – hypoosmotic stress	This study	EMD-19158
Focused map of the inner ring segment of the *D. discoideum* NPC – control condition	This study	EMD-51989
Focused map of the cytoplasmic ring segment of the *D. discoideum* NPC – control condition	This study	EMD-51990
Focused map of the nuclear ring segment of the *D. discoideum* NPC – control condition	This study	EMD-51991
Focused map of the lumenal ring segment of the *D. discoideum* NPC – control condition	This study	EMD-51992
Focused map around the basket connection of the *D. discoideum* NPC – control condition	This study	EMD-51993
Focused map of the inner ring segment of the *D. discoideum* NPC – hyperosmotic stress	This study	EMD-51994
Focused map of the cytoplasmic ring segment of the *D. discoideum* NPC – hyperosmotic stress	This study	EMD-51995
Focused map of the nuclear ring segment of the *D. discoideum* NPC – hyperosmotic stress	This study	EMD-51996
Focused map of the lumenal ring segment of the *D. discoideum* NPC – hyperosmotic stress	This study	EMD-51997
Focused map around the basket connection of the *D. discoideum* NPC – hyperosmotic stress	This study	EMD-51998
Focused map of the inner ring segment of the *D. discoideum* NPC – hypoosmotic stress	This study	EMD-51999
Focused map of the cytoplasmic ring segment of the *D. discoideum* NPC – hypoosmotic stress	This study	EMD-52000
Focused map of the nuclear ring segment of the *D. discoideum* NPC – hypoosmotic stress	This study	EMD-52001
Focused map of the lumenal ring segment of the *D. discoideum* NPC – hypoosmotic stress	This study	EMD-52002
Focused map around the basket connection of the *D. discoideum* NPC – hypoosmotic stress	This study	EMD-52003
80S *D. discoideum* ribosome ~1 min hyperosmotic stress	This study	EMD-52057
80S *D. discoideum* ribosome ~1 min hypoosmotic stress	This study	EMD-52058
Fluorescence microscopy data	This study	https://doi.org/10.5281/zenodo.14142946
Experimental models: Cell lines		
D.discoideum: AX2-214	dictyBase, Depositor Guenter Gerisch	DBS0235534
Human: Flp-In T-Rex 293 cell line	Thermo Fisher Scientific (Invitrogen)	N/A
Experimental models: Organisms/strains		
D. discoideum GFP-Nup62	Beck[102]	N/A

(*Continued on next page*)

Continued

REAGENT or RESOURCE	SOURCE	IDENTIFIER
D. discoideum GFP-Ran	Beck[102]	N/A
D. discoideum GFP-Nup62, H2B-mCherry	This study	N/A
Recombinant DNA		
pPI420	Paschke et al.[103]	Addgene plasmid # 113230
pLVX-EF1alpha-SARS-CoV-2-orf6-2xStrep-IRES-Puro	Gordon et al.[104]	Addgene plasmid # 141387
pcDNA3.1(-)	Thermo Fisher Scientific (Invitrogen)	N/A
pcDNA3.1_Orf6-sfGFP	This study	pMB981
Software and algorithms		
Fiji – ImageJ	Schindelin et al.[105]	https://github.com/fiji/fiji
3D ImageJ Suite	Ollion et al.[106]	https://mcib3d.frama.io/3d-suite-imagej/
Microsoft Excel	Microsoft	https://www.microsoft.com/en-us/microsoft-365/excel
GraphPad Prism 9	GraphPad	https://www.graphpad.com/
SerialFIB	Klumpe et al.[107]	https://github.com/sklumpe/SerialFIB
SerialEM (version 3.8.1 - version 4.0.1)	Mastronarde[108]	https://bio3d.colorado.edu/SerialEM/
IMOD	Kremer et al.[109]	https://bio3d.colorado.edu/imod/
Matlab	The MathWorks, Inc.	https://www.mathworks.com/products/matlab.html
novaCTF	Turoňová et al.[110]	https://github.com/turonova/novaCTF
WARP	Tegunov and Cramer[111]	https://github.com/warpem/warp
Relion 3.1	Zivanov et al.[112]	https://github.com/3dem/relion
M	Tegunov et al.[113]	https://github.com/cramerlab/warp
novaSTA	Turoňová et al.[114]	https://github.com/turonova/novaSTA
STOPGAP	Wan et al.,[115] Wan et al.[116]	https://github.com/wan-lab-vanderbilt/STOPGAP
dynamo2m toolbox	Burt et al.[117]	https://github.com/alisterburt/dynamo2m
ArtiaX	Ermel et al.[118]	https://github.com/FrangakisLab/ArtiaX
Chimera / ChimeraX	Pettersen et al.,[119] Goddard et al.[120]	https://www.cgl.ucsf.edu/chimerax/
MAFFT	Katoh et al.[121]	https://www.ebi.ac.uk/jdispatcher/msa/mafft
HMMER 3.1b2	Finn et al.[122]	http://hmmer.org/
AlphaFold	Jumper et al.,[56] Evans et al.[57]	https://github.com/google-deepmind/alphafold
AlphaPulldown	Yu et al.[123]	https://github.com/KosinskiLab/AlphaPulldown
Colabfold	Mirdita et al.[124]	https://github.com/sokrypton/ColabFold
Foldseek	van Kempen et al.[58]	https://search.foldseek.com/search
Assembline	Rantos et al.[125]	https://www.embl-hamburg.de/Assembline/
fdrtool R-package	Strimmer[126]	https://cran.r-project.org/web/packages/fdrtool/index.html
Integrative Modeling Platform (IMP) version 2.15	Webb et al.[127]	https://integrativemodeling.org/
Python Modeling Interface (PMI)	Saltzberg et al.[128]	https://github.com/salilab/pmi
GROMACS	Abraham et al.[129]	https://www.gromacs.org/
PI-score	Malhotra et al.[130]	https://gitlab.com/topf-lab/pi_score
CCP4	Winn et al.[131]	https://www.ccp4.ac.uk/

(*Continued on next page*)

Continued		
REAGENT or RESOURCE	SOURCE	IDENTIFIER
Rate4Site	Pupko et al.[132]	https://www.zoology.ubc.ca/%mayrose/cp/rate4site.html_
PISA	Krissinel and Henrick[133]	https://smb.slac.stanford.edu/facilities/software/ccp4/html/pisa.html
Python 3.88	Python.org	https://www.python.org/downloads/release/python-388/
anaconda 2021.05	Anaconda.org	https://docs.anaconda.com/
scipy 1.6.2	cipy.org	https://github.com/scipy/scipy
numpy 1.20.1	numpy.org	https://github.com/numpy/numpy
matplotlib 3.7.3	matplotlib.org	https://github.com/matplotlib/matplotlib
Adobe Illustrator 2023	Adobe	https://www.adobe.com/
Other		
Glass-bottom 35 mm dish	MatTek	P35G-1.5-10/14/20-C
CellASIC ONIX M04S-03 microfluidics plates	Merck Millipore	M04S-03-5PK
CellASIC® ONIX Microfluidic Platform	Merck Millipore	CAX2-S0000
Nikon Ti2 Eclipse Inverted Microscope	Nikon Instruments	Nikon Ti2-E
STELLARIS 5 Confocal Microscope	Leica Microsystems	Leica Stellaris 5
EM GP2 Automatic Plunge Freezer	Leica Microsystems	Leica GP2
Pelco easiGlow Glow Discharger Cleaning System	Ted Pella, Inc.	easiGlow
Quantifoil R 1/4, 200 Mesh, Au, SiO2 film	Quantifoil	N/A
Quantifoil R 2/2, 200 Mesh, Au, SiO2 film	Quantifoil	N/A
Quantifoil R 2/2, 200 Mesh, Au, holey carbon film	Quantifoil	N/A
Whatman filter paper #1	Whatman	WHA1001329
Aquilos2 dual beam cryo-FIB/SEM	Thermo Fisher Scientific	Aquilos2 cryo-FIB
Titan Krios G2 (300 kV cryo-transmission electron microscope)	Thermo Fisher Scientific	Titan Krios
K3 direct electron detector with BioQuantum imaging filter	Gatan	K3 with BioQuantum energy filter

EXPERIMENTAL MODEL AND STUDY PARTICIPANT DETAILS

Ax2-214 *D. discoideum* strain is a recommended wild type strain available via the dictyBase stock center (http://dictybase.org/; DBS0235534). HEK293 cells are standard human tissue culture cells which are available from multiple sources. Cell lines were grown and maintained according to standard protocols as further described in the method details section. More specialized *D. discoideum* strains used in the study will also be distributed without restriction upon request to the lead contact.

METHOD DETAILS

Molecular biology and cell culture

The axenic *D. discoideum* strains used in this study were all generated from an Ax2-214 background strain. GFP-Nup62 and GFP-Ran strains carried randomly integrated GFP-Nup62 or GFP-Ran with G418/neomycin resistance cassette.[102,134] H2B-mCherry was stably integrated at the *act5* locus of Ax2-214 or GFP-Nup62 strains respectively and selected with 50 μg/mL HygromycinB (Sigma Aldrich) using available genetic engineering tools and electroporation protocols for *D. discoideum* cells.[103] pPI420 for integration was a gift from Rob Kay (Addgene plasmid #113230; http://n2t.net/addgene:113230; RRID: Addgene_113230). *D. discoideum* cells were grown as described previously[50] in HL5 medium (Formedium) with 50 μg/mL ampicillin and additional antibiotic selection with 20 μg/mL geneticin G418 (Sigma Aldrich) or 50 μg/mL HygromycinB (Sigma Aldrich) at 20 ± 2 °C. Cells were kept either as adherent cells in sub-confluent conditions or as suspension culture at cell density between 1 x10^5 cells/ml to 4 x10^6 cells/ml. Cells were sub-cultured for a maximum of four weeks before re-growing them from cryo-stocks. HEK293 Flp-In T-REx cells (Invitrogen) cells were grown in Dulbecco's modified Eagle's medium (Thermo Fisher Scientific) with 10% fetal bovine serum and penicillin-streptomycin in a 5% CO_2 humidified incubator at 37 °C. pLVX-EF1alpha-SARS-CoV-2-orf6-2xStrep-IRES-Puro was a gift from Nevan Krogan (Addgene plasmid # 141387).[104] Orf6 was cloned into a pcDNA3.1 backbone containing a c-terminal sfGFP using Gibson Assembly and confirmed by sequencing.

Fluorescence Microscopy

D. discoideum cells were adjusted to a concentration of 2-3 x10^5 cells/ml and allowed to adhere to 35 mm dishes with 14 mm cover glass No 1.5 (Mattek) for 2-4 hrs.

Fluorescence images shown in Figure 1A were acquired using a Nikon Ti2 epifluorescence microscope with a 100x NA=1.49 TIRF objective, equipped with a SOLA light engine (Lumencor), an Orca flash 4.0 LT camera (Hamamatsu), and GFP/FITC and TRITC/CY3 filtercubes (Nikon). The adherent cells on the cover glass were imaged at room temperature. Focal stacks were acquired of cells with a step size of 0.5 μm. Cells were treated for approximately ~3 min with either HL5 medium + 0.4 M sorbitol or with double distilled water before taking representative images displayed in Figure 1A. Equatorial slices through the cell's nuclei are displayed and brightness and contrast of images was adjusted using Fiji.[105]

Time-lapse imaging of cells was performed at room temperature with a Leica Stellaris 5 microscope equipped with white light laser, with an HC PL APO CS2 63x water objective with NA=1.20 and operated in resonance scanning mode. For initial assessment and testing imaging parameters, cells were adhered to Mattek dishes as described above and osmotically stressed by manually exchanging HL5 medium with either HL5 medium + 0.4 M sorbitol (hyper-OS) or with double distilled water (hypo-OS). In order to reliably determine nucleus and cell size, *D. discoideum* cells were seeded in CellASIC ONIX M04S-03 microfluidics plates at a density of 1x10^6 cells/ml. Using the CellASIC ONIX2 microfluidics device cells were either imaged without media exchange (control cells) or with one minute flow of HL5 medium at 34.5 kPa, followed by six minutes flow with respective osmotic treatment solution. In order to monitor buffer exchange, additional buffer exchange experiments for each microfluidics plate were performed again separately with 500K-FITC-dextran (Sigma Aldrich) at a final concentration of 0.2 μM to the treatment solution. All GFP-labeled proteins and fluorescent dextran were excited at 489 nm and emission detected at 500-575 nm, mCherry-labeled H2B was excited at 587 nm and emission detected at 595-670 nm on HyD detectors in bidirectional scanning mode with line averaging. Focal stacks of cells were acquired as 12-bit images with a pixel size of 82.5 nm, z step size of 0.5 μm and z stack sizes of 10-16 μm, resulting in time intervals of 2, 3 or 5 sec between individual stacks. Time-lapse experiments were usually acquired for about 5-10 min. For measuring nuclear permeability of 500K-FITC-dextran during digitonin-induced cell rupture and nuclear volume change, cells adhered to Mattek dishes were exposed to HL5 +0.4 M sorbitol + 20 μg/ml digitonin + 0.2 μM 500K-FITC-dextran while imaging with the settings described above.

HEK293 were seeded at a concentration of 1x10^5 cell/ml in glass-bottom dishes (Mattek) and allowed to adhere overnight. Cells were then transiently transfected using Lipofectamine 3000 (Life Technologies) with pcDNA-3.1-SARS-CoV2-Orf6-sfGFP plasmid DNA. After 48 hrs of transfection, cells were imaged as previously described with a Stellaris 5 microscope (Leica) and stage incubator (Okolab) at 37 °C. First, cells were stained with 2μM Hoechst-33342 in DMEM for 10-15 min. Cells were then imaged before and after applying hypoosmotic stress by manually exchanging DMEM medium to 0.33x DMEM diluted with double distilled water. Manual application of stress was required due to technical limitations of the setup and resulted in a time gap of approximately 20 sec until the first stack could be acquired after applying osmotic stress.

Cell and nuclear size determination

Image segmentation and volume measurements were done in Fiji.[105] To estimate nuclear size, raw images were cropped to contain one cell of interest, then gaussian filtered and a threshold with the Default method was applied for segmentation in Fiji[105] using the 3D ImageJ Suite.[106] For cellular size estimation images were additionally filtered with median filter before thresholding with the Otsu method and segmentation in Fiji using 3D manager. Cells or nuclei that moved out of the field of view or started to touching each other during the time course of acquisition were excluded from analysis. For monitoring the buffer exchange with 500K-FITC-dextran in the microfluidics chamber, the mean background fluorescence of five squares with 60-pixel box size in empty regions of the raw image was measured over time.

Dextran permeability was directly assessed within the time frame of 1 min before cell rupture and 1 min after rupture. As cells randomly ruptured within the field of view after treatment, 10 min time lapse confocal stacks were taken and individual cells upon rupture were analysed. For this, nuclear size was estimated from segmentations of the H2B-mCherry signal as described above with a manual threshold (lower limit of 170) due to the increased background fluorescence due to addition of 500K-FITC-dextran. The nuclear size was determined from segmentations in Fiji[105] using the 3D ImageJ Suite.[106] The mean 500K-FITC-dextran signal of the nucleus and whole cell was measured for a manually selected area covering the equatorial plane of the nucleus or whole cell. For HEK293 cells, nuclei were segmented based on their Hoechst signal, after filtering using gaussian and median filtering and additionally using the 'fill holes' function in Fiji for the segmentation. All volume estimates and mean grey values were plotted using Prism9 software and to determine shrinkage and expansion, data was fitted using plateau followed by one phase exponential decay function in Prism9.

Cryo-EM sample preparation

EM support grids (Au grids 200 mesh, carbon or SiO_2 foil, R2/2 or R1/4, Quantifoil) were glow discharged with a Pelco easiGlow for 90 sec at 15 mA. Exponentially growing *D. discoideum* GFP-Nup62 cells were adjusted to a concentration of 2 - 3 x 10^5 cells/ml. A droplet of 100 μl cell suspension was pipetted on the foil side of the grids and cells were allowed to attach to the grids for 2 - 4 hrs. Cells were vitrified by plunge freezing into liquid ethane using a Leica EM GP2 plunger. For treated cells, the media was exchanged for one minute or in few cases for five minutes prior to plunge freezing with either HL5 with 0.4 M sorbitol (hyper-OS) or with double distilled water (hypo-OS).

Lamellae were prepared by cryo-FIB milling using an Aquilos2 microscope (Thermo Fisher Scientific) as described previously.[50] In short, samples were coated with an organometallic platinum layer using a gas injection system for ~10 sec and additionally sputter coated with platinum at 1 kV and 10 mA current for ~10 sec. SEM imaging was performed with 2 - 10 kV and 13 pA current to monitor the milling progress. Milling was performed stepwise with a gallium ion beam at 30 kV while reducing the current from 500 pA to 30 pA. Final polishing was performed with 30 pA or in some cases with 10 pA current to reach a target lamellae thickness between 130 - 200 nm. Some lamellae were sputter coated with platinum after polishing for 1 or 2 sec at 1 kV and 10 mA. For some of the samples, the rough milling step to a lamella thickness of approximately 600 nm was carried out in an automated workflow using SerialFIB,[107] while final polishing was then performed manually as described.

Cryo-ET acquisition

A cryo-ET dataset of *D. discoideum* GFP-Nup62 cells grown in HL5 medium as control condition was acquired in five independent 48-hour microscope sessions from 14 grids from overall 9 independent plunge freezing sessions and with a total of 87 cryo-FIB milled lamellae (Table S1). The control dataset is published as 'dataset 1' in the context of ribosome translational states *in situ*[50] and available through EMPIAR-11845. The hyper-OS dataset was acquired in six microscope sessions from 11 grids with a total of 55 cryo-FIB milled lamellae (Table S1) and is available through EMPIAR-11943. The hypo-OS dataset was acquired in four microscope sessions from 7 grids with a total of 61 cryo-FIB milled lamellae (Table S1) and is available through EMPIAR-11944. All data were collected at 300 kV on a Titan Krios G2 microscope (Thermo Scientific) equipped with a Gatan BioQuantum-K3 imaging filter in counting mode. For each grid, montaged grid overviews were acquired. Then montages of individual lamellae were taken with 3.9 nm or 2.8 nm pixel size. Tilt series were acquired using SerialEM (version 3.8.1 - version 4.0.1)[108] in low dose mode as ~6K x 4K movies of 10 frames per tilt image, and motion-corrected in SerialEM on-the-fly. The magnification for projection images of 42000x corresponded to a pixel size of 2.176 Å. Tilt series acquisition started from the lamella pretilt of ± 8° and a dose symmetric acquisition scheme[135] with 2° increments grouped by 2 was applied, resulting in 59 - 61 projections per tilt series with a constant exposure time and total dose between 132 - 150 e^- per $Å^2$. The energy slit width was set to 20 eV and the nominal defocus was varied between -2.5 to -5 μm. The initial dose rate on the detector was targeted to be between ~10 - 20 e^- /px/sec.

Tomogram reconstruction

The motion-corrected tilt series were filtered for dose exposure as previously described[136] using a Matlab implementation that was adapted for tomographic tilt series.[137] Poor quality projections were removed after visual inspection. The dose-filtered tilt series were aligned in IMOD (versions 4.10.9 and 4.11.5)[109] with patch-tracking using four-fold binning and a patch size of 500-600 pixel with 0.8 patch overlap low frequency roll-off sigma 0.01 and high frequency cutoff radius between 0.07 - 0.2. After initial assessment, contours were broken and tracks that were visually not well aligned with respect to the remaining tracks were removed. Tomograms were reconstructed as back-projected tomograms with SIRT-like filtering of 10 iterations at a binned pixel size of 8.7 Å for initial tomogram inspection. For NPC STA and ribosome template matching, 3D CTF-corrected back-projected tomograms were generated using NovaCTF.[110] For ribosome averaging and classification, for compatibility with Relion 3.1[112] and M,[113] the tilt series were reprocessed in Warp[111] with the alignment obtained from IMOD.

Ribosome template matching

Template matching was done in STOPGAP[115,116] using the *D. discoideum* ribosome map (EMD-15808) as template, resampled to a pixel size of 1.306 nm which corresponding to binning factor 6 of the dataset. Template matching was performed on 3D CTF-corrected back-projected tomograms with an angular search of 20°. The top 1000 cross-correlation peaks were extracted from each tomogram. The obtained coordinate and angles for each dataset were converted into Warp-compatible star files using the dynamo2m toolbox.[117]

Ribosome classification and ribosome analysis

Classification was performed as previously described.[50] In short, bin4 (8.704 Å/px) subtomograms were classified in Relion 3.1[112] to filter out non-ribosomal particles such as membranes and other granular structures. This yielded 51990 / 25830 ribosomal particles (hyper-OS / hypo-OS), which were then again classified to distinguish between cytosolic (50040 particles for hyper-OS, 23470 for hypo-OS) and membrane-bound 80S ribosomes (1950 particles for hyper-OS, 2360 for hypo-OS). For all tomograms, we performed manual cleaning of the cytosolic ribosomes in ArtiaX[118] resulted in 49667 (hyper-OS) and 22999 (hypo-OS) cytosolic ribosomes that were used for M refinement and classification. Then, unbinned (2.176 Å/px) subtomograms (of the cytosolic 80S ribosomes were refined in Relion 3.1. The positions were then imported into M[113] to perform multi-particle refinement of the tilt series and the ribosome. Geometric and CTF parameters were sequentially refined. This resulted in consensus maps of the cytosolic 80S ribosome after hyper-OS (4.5 Å resolution) and hypo-OS (5.9 Å resolution). In order to estimate ribosome concentration, for each cytosolic and membrane-bound 80S ribosome position, the number of ribosomes contained in a 100 nm large box was determined. For each dataset, the containing ribosome number of each box was displayed in a histogram (Figure 2C). Focused classification and state assignment was performed as described.[50] First, with a smooth shape mask covering the A-, P-, E-site tRNA positions (10 classes, T=4, 35 iterations). The refinements of each class were then subjected to a second round of focused classification (5 classes, T=5, 35 iterations) with a smooth shape mask covering the factor binding site next to the A-site tRNA position. The resulting classes were all

refined, and atomic models of 80S ribosomes with elongation factors and tRNAs bound[138–141] were rigid body fitted into the refined maps to identify different states. Resulting states and occupancy were compared to the previously published data.[50]

NPC particle selection and subtomogram averaging

Positions of NPCs were manually selected as described previously[60] and already during visual inspection of tomograms. NPCs that were located close to the lamella border and thus only minimally contained in the lamella volume were not selected for STA.

For NPC STA, 3D CTF-corrected back-projected tomograms were generated using NovaCTF.[110] Extraction of particles, subtomogram alignment and averaging was in general performed using NovaSTA[114] followed by final alignment using STOPGAP.[115] NPC averaging was performed as described previously.[18,26] In detail, an initial average of the whole NPC was obtained using NovaSTA. From this, coordinates of the subunits were determined based on 8-fold symmetry. These positions were used to obtain the average structure of the asymmetric unit of the NPC. The extracted asymmetric units were used for further alignment using a spherical mask covering the whole unit. At this point, the particle positions that were generated based on 8-fold symmetry but not contained in the lamella volume, were manually cleaned from the particle list using the ArtiaX plugin[118] for ChimeraX.[120] Initially all datasets were combined to obtain the overall *D. discoideum* NPC structure. Then averaging was again performed for each dataset separately (control, hyper-OS and hypo-OS) to generate low resolution maps, focused maps and composite NPC maps for each condition. For subtomogram averaging of individual rings, particle positions were re-centered to the respective area (CR, IR, NR, LR, basket connection at NR, basket filaments) based on their position in low resolution maps. STA was further carried out for individual rings with 4- or 2-fold binned subtomograms and elliptical masks around each area of interest in NovaSTA.[114] Final alignment was carried out using STOPGAP.[115] The individual ring averages were b-factor sharpened empirically and low-pass filtered. The individual ring maps used were determined at 4-fold binning, as 2-fold binning did not result in better resolved maps based on FSC evaluation and visual inspection. To generate 8-fold symmetric composite NPC maps, the final averages of individual ring maps were fitted to the lower resolution asymmetric subunit average. The density value of all individual ring maps was adjusted to values to represent features of the composite average at a common threshold level. The 8-fold symmetric composite was then produced by applying symmetry based on the coordinates used for splitting the initial NPC average into asymmetric units.

NPC diameter measurements

NPC diameters were measured based on the coordinates obtained from STA maps of individual rings using previously published MATLAB scripts and as described previously.[26] Using IMOD, the features of interest in the STA map were identified and coordinates were offset by the shift between the center and the feature of interest. Only NPCs with more than five subunits were considered for diameter measurement of NPCs. As previously described, for each individual NPC, vectors were determined that connected opposing subunits. The point to which the distance of all vectors is minimal was defined as the NPC center, from which the distance to each subunit was reported as the NPC radius and the NPC diameter for each subunit was calculated. Each grid, since frozen and treated separately, was thus treated as one replicate. For each grid, the mean NPC diameter was calculated (black data points), when more than three individual NPC measurements per grid were possible (Figures 5C–5E). Individual NPC measurements were plotted as smaller colored data points. Data was plotted using Prism9 software. Statistical significance was tested using ordinary one-way ANOVA in Prism9.

NE segmentation, NPC diameter correlation and NPC density calculation

3D CTF-corrected tomograms as described above at binning factor 8 with a pixel size of 1.74 nm were filtered in IMOD using the SIRT-like filtering option. Subsequently, the NE lumen including its membranes was manually segmented from tomograms using the Amira-Avizo software in approximately every 10 slices and then interpolated. Tomograms with limited visibility of the NE membrane, either as result of osmotic treatment or because of the tilted membrane orientation towards the lamella plane, were excluded from segmentation analysis. For segmentation, we used 34 tomograms from 7 grids for control, 21 tomograms from 4 grids for hyper-OS and 34 tomograms from 4 grids for hypo-OS conditions. For each segmented NE volume, a surface model was generated. The volume comprising the NE lumen, was normalized to the mean NE surface area of the INM and ONM of the segmented NE volume. This ratio served as an approximation of the mean NE thickness in each tomogram. For each grid, the mean NE volume to surface area ratio (black data points), and individual tomogram values (smaller colored data points) were plotted in Prism9 (Figure 5F). Statistical significance was tested using ordinary one-way ANOVA in Prism9. By integrating the STA NPC and NE segmentation data, we calculated the density of asymmetric NPC subunits per NE surface area, which is displayed as number of NPC per μm^2 assuming 8-fold symmetry of the NPCs (Figure 5H). For confocal stacks of control cells and cells during hypoosmotic stress we estimated an average nuclear volume of 20.1 μm^3 (SD = 6.3, n = 50 cells) and 26.0 μm^3 (SD = 8.0, n = 17 cells) respectively. Assuming spherical geometry of the nucleus, this resulted in a surface area of 35.7 μm^2 and 42.4 μm^2 respectively. Using the average surface of the NE, we extrapolated the NPC number per *D. discoideum* nucleus to between 380 – 540.

Bioinformatics identification of *D. discoideum* Nups

The Nups have been identified by a sequence profile search against the *D. discoideum* proteome, followed by validation with reverse sequence searches and structure prediction. To build the query profile, each human Nup was used to retrieve orthologous proteins from the Eggnog database.[142] To assemble and build multiple sequence alignment (MSA) from the list of proteins, the retrieved

protein sequences were aligned using the MAFFT algorithm[121] and adjusted, e.g., trimmed to retain conserved domains or motifs but to remove variable regions. The adjusted sequences were re-aligned, using local or global alignment dependent on the presence of conserved elements, again within the MAFFT environment. The resulting MSA was used to create a Hidden Markov Model (HMM) profile using the hmmbuild and hmmconvert tools provided in the HMMER 3.1b2 package.[122] The hmmsearch tool was then used to search the *D. discoideum* proteome (UNIPROT GCA_000004695.1), and the first two hits with the best E-value were considered potential Nup candidates.

The candidates were then validated by additional analyses to confirm orthology or to discriminate between alternative hits. The analyses included a reverse search using phmmer against proteome sequence databases of humans and other species presenting conserved Nups. Further orthology assessment was carried out by an HMM-HMM profile comparison using the HHPRED suite and predicted secondary structure similarity comparison with proteins deposited in the Protein Data Bank,[143] a search for transmembrane domains, and other conserved motifs/domains typical for Nups. The reverse search was also performed by (BLASTp) searches against SwissProt and nr databases.[144,145] Finally, the sequences were validated by the similarity of resulting AlphaFold models to orthologous Nups. The final Nup sequence assignments are summarized in Table S3.

Structural modeling of Nups and NPC subcomplexes

The structures of individual Nups and NPC subcomplexes were modeled using AlphaFold[56,57] available through AlphaPulldown[123] and Colabfold.[124] The max_recycles parameter was set between 12 to 48, depending on the subcomplex, to ensure convergence. The following models were generated using AlphaPulldown: Nup54 (aa. 180-440)-Nup58 (aa. 160-350)-Nup62 (aa. 520-709)-Nup93 (aa. 1-110), Nup160 (aa. 1000-1791)-Nup85-Seh1-Nup43, Nup160 (aa. 1120-1791)-Nup96-Sec13, Nup107-Nup96, Nup160 (aa. 1-1200)-Elys (aa. 1-1100), Nup35 (aa. 377-460) homo-dimer, Nup93 (aa. 170-979)-Nup35 (aa. 1-360), Nup107-Nup133 (aa. 490-1206), Aladin-Ndc1, Nup205_N-Nup205_C-Nup93 (aa. 100-170), Nup188-Nup93 (aa. 100-170), Nup155, Nup155 (aa. 1176-1575)-Nup98 (aa. 800-1000), Nup214 (aa. 601-901)-Nup88-Nup62 (aa. 521-709), Nup160 (aa. 1-1430)-Elys (aa. 590-1170)- Nup96 (707-889), Nup210 (aa. 1-500) homo-dimer, Nup210 (aa. 1151-1610), Nup210 (aa. 355-785), Nup210 (aa. 680-1150), Nup210 (aa.1050-1355) and Nup210 (aa. 1355-1825), and Nup358 (aa. 1-780) (Figure S3).

The quality of the AlphaFold models was assessed using the scores provided by AlphaFold: the predicted local-distance difference test (pLDDT), which predicts the local accuracy, and the Predicted Aligned Error, which assesses the relative orientation of the proteins and protein domains. In addition, the models of the *D. discoideum* Nups were used to search for similar folds in PDB using Foldseek[58] to validate that the predicted *D. discoideum* Nups have the same fold as the already known Nups. The TM-score and RMSD between the query and the target structure were additionally calculated using TM-align server.[146] Physical parameters of protein-protein interfaces modelled by AlphaFold were calculated using PI-score pipeline[130] using CCP4,[131] Rate4Site,[132] and PISA[133] programs included in the pipeline. The models were minimized using GROMACS[129] prior to analysis.

Fitting of atomic structures to cryo-ET maps

To generate the model of the asymmetric unit of the *D. discoideum* NPC, we used the model of the human NPC (PDB 7R5J)[13] and the model of the CR of the *X. leavis* NPC (PDB 7VOP)[147] as templates. First, we fitted the IR and LR of the human NPC into the map of the IR and LR of the *D. discoideum* NPC. Then we fitted the fragments of the CR of the human and *X. leavis* NPC into the *D. discoideum* CR map and the fragments of the human NR model into the *D. discoideum* NR map. Finally, we superposed AlphaFold models of the *D. discoideum* NPC subcomplexes to the human/*X. leavis* model, and optimized the fits of the *D. discoideum* NPC subcomplexes into the map of the *D. discoideum* NPC using ChimeraX.[120] Systematic fitting of the Nup133 (aa. 490-1206), Nup107 (aa. 708-985)-Nup133 (aa. 490-1206) was performed using the full cryo-ET map of the NR (Figures S5A, S5B, S5E, and S5F) and Nup358 (aa. 1-780) using the difference maps of the CR obtained after subtracting the density of Y-complexes (Figures S5C and S5D).

Systematic fitting

We used the previously published procedure for systematic fitting[18,148,149] to locate the atomic structures in the cryo-ET maps. Before fitting, all the high-resolution structures were filtered to 15 Å. The resulting simulated model maps were subsequently fitted into individual ring segments of cryo-ET maps by global fitting as implemented in UCSF Chimera[119] using scripts in Assembline[125] All fitting runs were performed using 100,000 random initial placements, with the requirement of at least 60% of the simulated model map to be covered by the cryo-ET density envelope defined at a low threshold. For each fitted model, this procedure resulted in ~100 to 3,000 fits with nonredundant conformations upon clustering. The cross-correlation about the mean (cam score, equivalent to Pearson correlation) score from UCSF Chimera[119] was used as a fitting metric for each atomic structure, similarly to our previously published works. The statistical significance of every fitted model was evaluated as a P-value derived from the cam scores. The calculation of P-values was performed by first transforming the cross-correlation scores to z-scores (Fisher's z-transform) and centering, from which subsequently two-sided P-values were computed using standard deviation derived from an empirical null distribution [based on all obtained nonredundant fits and fitted using fdrtool[126] R-package]. Finally, the P-values were corrected for multiple testing with Benjamini-Hochberg procedure.[150]

Modeling of the *D. discoideum* NPC scaffold

To assemble the model of the entire NPC scaffold we used the integrative modeling software Assembline[125] which is based on Integrative Modeling Platform (IMP) version 2.15[127] and Python Modeling Interface (PMI).[128]

In addition to using models of subcomplexes as rigid bodies for fitting in the modeling, several inter-subunit interfaces (Nup107-Nup133, Nup107-Nup96, Nup160-Nup85) and inter-domain interfaces of Nup210 were restrained by elastic distance network derived from AlphaFold models, overlapping and bridging the already fitted models. During the refinement, the structures were used as rigid-bodies and simultaneously represented at two resolutions: Cα-only representation and a coarse-grained representation, in which 10-residue fragments were represented as a single bead. The Cα-only representation was used for all restraints except for the EM fit restraint.

The structures of individual rings (CR, NR, and IR together with LR) were optimized using the refinement step of Assembline to optimize the fit to the map, minimize steric clashes, and ensure connectivity of the protein linkers. The scoring function for the refinement comprised the EM fit restraint, clash score (SoftSpherePairScore of IMP), connectivity distance between domains neighboring in sequence, and elastic network restraints derived from the subcomplexes modeled with AlphaFold. The final atomic structures were generated based on the refinement models by back-mapping the coarse-grained representation to the original AlphaFold atomic models. The stereochemistry of the final models was optimized using steepest descent minimization in GROMACS.[129]

The structures of the NPC in the constricted and dilated states were generated by fitting the model of the asymmetric unit of the *D. discoideum* NPC into the EM map of the constricted and dilated NPC and refining using Assembline.

Mathematical model of fluid flow across the NPC and NE during osmotic stress

In our model of fluid flow across the NPC, we assumed an idealized spherical cell containing a spherical nucleus with radii r_C and r_N, respectively. We assumed each compartment to be well mixed with osmolyte concentrations C_C, C_N and C_O, respectively, in the cytosol (C), the nucleus (N), and outside (O) of the cell. We set the water permeability of the PM at a value typical for cells, 35 $\mu m \cdot s^{-1}$[65,66] (Figure 6C). For the more loosely packed NE,[66–70] we assumed a permeability in the range of $35 - 700\ \mu m \cdot s^{-1}$, with a typical value of $350\ \mu m \cdot s^{-1}$. We included tension contributions to the pressure in the NE only under hypoosmotic conditions, assuming the NE to be relaxed under hyperosmotic conditions. Certain volume fractions inside the cytosol and the nucleus were excluded from the effective solvent volumes undergoing changes osmolarity during the experiment.[151,152] We estimated that there are ~450 NPCs per cell (Figure 5H).

The osmotic pressure Π across a semi-permeable membrane is proportional to the difference in osmolyte concentration ΔC,

$$\Pi = iRT\Delta C \propto \Delta C \quad \text{(Equation 1)}$$

where i, R, and T denote the van 't Hoff index, ideal gas constant and temperature, respectively. The osmotic pressure drives a water flux through the membrane[153]:

$$\tilde{J}_{W_{C\to O}} = \frac{k_{mem}}{iRT}\left(\Delta\Pi - \Delta P_{hydro}\right) = k_{mem}(C_O - C_C) + \frac{k_{mem}}{iRT}\Delta P_{hydro} \quad \text{(Equation 2)}$$

where $\tilde{J}_{W_{C\to O}}$ is the number of translocated water molecules (in unit of mole) per unit time and unit area from the cytosol to the outside; k_{mem} is the membrane water permeability; and $\Delta P_{hydro} = P_O - P_C$ is the difference in the hydrostatic pressure between the nucleus and cytosol. Without hydrostatic pressure change across the PM, $P_O \approx P_C$, the flux from the cytosol to the outside (in unit of mole per unit time) is:

$$J_{W_{C\to O}} = 4\pi r_C^2 k_{mem}(C_O - C_C) \quad \text{(Equation 3)}$$

We treat the NE as a single entity, ignoring its small luminal volume. The flux of water from the nucleus to the cytosol then becomes

$$J_{W_{N\to C}} = 4\pi r_N^2 k_{mem-NE}\left[(C_C - C_N) + \frac{P_\sigma(r_N)}{iRT}\right] \quad \text{(Equation 4)}$$

where k_{mem-NE} denotes the overall water permeability across the NE and $P_\sigma(r_N)$ (Equation 5) denotes the hydrostatic pressure due to the tension in the NE (σ_{NE}), which accumulates as the NE expands. For expanding nuclei, the NE tension cannot be neglected due to the support of its lamina, which provides the NE a larger resistance against expansion compared to the PM. Note when $C_N > C_C$, the sign of the first term is negative while the second term is positive, hence the NE tension would retard the water diffusing into the nucleus from the cytosol, across the NE. For the pressure created by NE tension we use Deviri et al.[81]

$$P_\sigma(r_N) = \sigma_{NE}\frac{4\pi\left(r_N^2 - R_N^2\right)}{\frac{4\pi r_N^3}{3}} = \frac{3\sigma_{NE}}{r_N}\left(1 - \frac{R_N^2}{r_N^2}\right)\Theta(r_N - R_N) \quad \text{(Equation 5)}$$

where R_N denotes the radius of the relaxed NE and the Heaviside function Θ ensures that tension acts only when the NE is expanded, $r_N > R_N$. The value of σ_{NE} can be estimated from the experiment by equating the osmotic and tension pressure during the steady state after the hyposmotic shock. Here, σ_{NE} was estimated to be 0.05Nm^{-1}, with a strict upper bound of $\approx 0.1\text{Nm}^{-1}$.

Exchange between the cytosol and the nucleus are further mediated across the NPCs, through which bulk flow (translocation of both the water and solute molecules; $J_{NPC} = J_{NPC_W} + J_{NPC_S}$), is allowed. Due to the concentration gradient across the NE, J_{NPC} is driven by both the hydrostatic pressure and chemical potential. Note that the former is partly a consequence of the NE tension, which causes efflux ($J_{NPC_\sigma} = k_\sigma P_\sigma(r_N)$) when $r_N > R_N$. Another contribution to the former is the accumulation of the osmotic pressure across

the NE (Equation 1), and the consequent hydrostatic pressure induces the flux from low to high concentration via NPCs, analogous to the "balloon effect"; J_{NPC_W} has the same sign as $J_{W_{N\to C}}$ and if we neglect the concentration gradient within the NE, such hydrostatic pressure (due to the build-up of osmotic pressure) is proportional to $C_C - C_N$, ignoring the NE as a separate compartment. In the following, we also ignore diffusive water and solute transport across the NPC, which is overwhelmed by hydrodynamic flow. We also assume that the solute volume fraction is small compared to the water volume fraction, $\varphi_S \ll \varphi_W$. Consequently, differential equations for each volume compartment can be formulated based on the expressions for the respective fluxes.

In time dt, the volume of the cell changes as,

$$dV_{Cell} = \nu_W dN_{W_{Cell}} + \nu_S dN_{S_{Cell}} \approx -\nu_W J_{W_{C\to O}}\, dt = -4\pi\nu_W k_{mem} r_C^2 (C_O - C_C)dt \quad \text{(Equation 6)}$$

where ν_W and ν_S are the molar volume of water and solute, respectively, and $N_{W_{Cell}}$ and $N_{S_{Cell}}$ are the total number of water and solute molecules inside the cell (in moles). The volume of the nucleus changes as

$$dV_N = \nu_W dN_{W_N} + \nu_S dN_{S_N} = -\nu_W \left(J_{W_{N\to C}} + J_{NPC_W}\right)dt - \nu_S J_{NPC_S} dt \approx -\nu_W dt \Big[(C_C - C_N) \times \left(4\pi k_{mem-NE} r_N^2 + k_{NPC_W}\right) + P_\sigma(r_N)\left(k_\sigma + \frac{4\pi r_N^2 k_{mem-NE}}{iRT}\right)\Big] \quad \text{(Equation 7)}$$

For the solute concentrations in each compartment, we use effective volumes obtained by subtracting excluded volumes (of organelles, genome, nucleoli etc.), which we estimated at 50% of the measured values before the osmotic shock: $V_{C-eff} = V_{Cell} - V_N - V_{C-exe} = 4\frac{\pi}{3}(r_C^3 - r_N^3) - V_{C-exe}$, and, $V_{N-eff} = V_N - V_{N-exe} = 4\frac{\pi}{3}r_N^3 - V_{N-exe}$. The concentrations at times $t+dt$ with small dt are then

$$C_C(t+dt) = \frac{N_{S_C}(t+dt)}{V_{Cell}(t+dt) - V_N(t+dt) - V_{C-exc}} \approx C_C(t) + \frac{J_{NPC_S} + C_C\nu_W\left(J_{W_{C\to O}} - \left(J_{W_{N\to C}} + J_{NPC_W}\right)\right)}{V_{C-eff}}dt \quad \text{(Equation 8)}$$

And similarly

$$C_N(t+dt) = \frac{N_{S_N}(t+dt)}{V_N(t+dt) - V_{N-exe}} \approx C_N(t) + \frac{C_N\nu_W\left(J_{W_{N\to C}} + J_{NPC_W}\right) - J_{NPC_S}}{V_{N-eff}}dt \quad \text{(Equation 9)}$$

We now rewrite the above expressions as differential equations for the concentrations and the radii of the spherical volumes:

$$\frac{dr_C}{dt} = -\nu_W k_{mem}(C_O - C_C) \quad \text{(Equation 10)}$$

$$\frac{dr_N}{dt} = -\frac{\nu_W(C_C - C_N)\left(4\pi k_{mem} r_N^2 + k_{NPC_W}\right)}{4\pi r_N^2} - \frac{\nu_W P_\sigma(r_N)}{4\pi r_N^2}\left(k_\sigma + \frac{4\pi r_N^2 k_{mem-NE}}{iRT}\right) \quad \text{(Equation 11)}$$

$$\frac{dC_C}{dt} = \frac{(C_C - C_N)}{V_{C-eff}}\left[k_{NPC_S} - C_C\nu_W k_{NPC_W}\right] + \frac{4\pi C_C\nu_W\left(k_{mem} r_C^2(C_O - C_C) - k_{mem-NE} r_N^2(C_C - C_N)\right)}{V_{C-eff}} - \frac{\nu_W P_\sigma(r_N)}{V_{C-eff}}\left(k_\sigma(C_C - C_N) + \frac{4\pi r_N^2 C_C k_{mem-NE}}{iRT}\right) \quad \text{(Equation 12)}$$

$$\frac{dC_N}{dt} = \frac{4\pi r_N^2 k_{mem-NE} C_N\nu_W(C_C - C_N)}{V_{N-eff}} + \frac{(C_C - C_N)}{V_{N-eff}}\left(C_N\nu_W k_{NPC_W} - k_{NPC_S}\right) + \frac{4\pi r_N^2 C_N\nu_W P_\sigma(r_N) k_{mem-NE}}{iRTV_{N-eff}} \quad \text{(Equation 13)}$$

A full list of the constants – together with the values used/estimated in this manuscript – in Equations 10, 11, 12, and 13 can be found in Table S2. The differential equations were solved numerically with a Runge Kutta-4 integrator.[154]

Porous flow model

Assuming a porous flow model, the fluid flux through the NPC satisfies Darcy's law[155,156],

$$J_{NPC} = k_{NPC_{\Delta P}}\Delta P = \frac{\pi R_{NPC}^2 k_{Darcy}}{\mu L}\Delta P$$

with μ the solvent viscosity. For cells undergoing hyperosmotic shock, the pressure difference ΔP across the NE is due to the accumulation of the osmotic pressure, Equation 1. The permeability of the porous medium k_{Darcy} can be related to critical radius of the tubules through the medium[73–77],

$$k_{Darcy} = c\varphi_s {r_{CR}}^2$$

where $c \approx 1$ is the relative path length and $\varphi_s \approx 0.5$ to 0.9 is the solvent volume fraction in the pore. In our estimates, we set $L = 100$ nm and μ to 10 times the water viscosity.[71,72]

Uncertainty estimation

Table S2 illustrates a complete list of input variables of the model, with the corresponding uncertainty ranges. Based on the second column entry of the input variables, the permeabilities of a single NPC during hypertonic and hypotonic shocks were determined to be $k_{NPC_W} \approx k_{NPC} \sim 6000\ \mu m^3 s^{-1}$ and $18000\ \mu m^3 s^{-1}$ ($J_{NPC} = v_W k_{NPC} \Delta C$), respectively, by performing a chi square test. The uncertainty in the NPC permeability associated with the uncertainty ranges of the individual non-experimentally predetermined input variables were numerically estimated. Considering that a monotonic change in most of the input variables individually causes a monotonic change in the NPC permeability, the overall uncertainty in the NPC permeability is numerically obtained to be a factor ~2. However, it is important to note that this seemingly large relative uncertainty is greatly reduced when the permeability k is converted into an effective pore radius r for Hagen-Poiseuille flow, $r \propto k^{1/4}$, or Darcy porous flow, $r \propto k^{1/2}$.

Compared to hyperosmotic stress, modelling the hypoosmotic stress is subject to a larger degree of uncertainty and error, especially for later time points. A typical example is illustrated in Figure S7C, in which the predicted r_C noticeably deviates from the experimental observation at late times. The major cause of this is the neglection of a PM tension building up as the cell expands. Relatedly, the chi square test for the hypotonic shock was performed for time up to 300 seconds in Figure S7. Furthermore, the modelled NE tension (Equation 5) is also subject to a certain degree of uncertainty (σ_{NE} in Table S2). The corresponding uncertainty in the NPC permeability was found to be $\approx 10\%$, which is small compared to the overall uncertainty (~factor 2).

QUANTIFICATION AND STATISTICAL ANALYSIS

Resolution of cryo-ET NPC maps were estimated using FSC 0.143 criterion using STOPGAP.[115] Fluorescence microscopy experiments to analyze *D. discoideum* cell and nuclear size were conducted with a minimum of three replicates and a total of 6 to 17 individual cells (n) as indicated. Cells could only be analyzed when nuclei or the whole cell volume could be separated from other cells and when cells did not move out of the field. Data was analyzed and the mean and standard deviation plotted in GraphPad Prism. NPC diameter measurements were performed from STA coordinates for individual subunits. Data from each grid was treated as separate experimental treatment. For control cells, data from 12 grids with more than three NPC diameter measurements (305 NPCs) was analyzed; for hyper-OS data from 8 grids (227 NPCs in total); for hypo-OS data from 6 grids (132 NPCs in total). The mean and 95% confidence intervals were plotted. Statistical significance was tested using ordinary one-way ANOVA, significance level: * $P<0.05$, ** $P< 0.01$, *** $P< 0.001$, P values are stated for non-significant results. For HEK293 nuclear size cells was only analyzed when nuclei could clearly be separated from nuclei of other cells. Experiments were conducted with a minimum of three replicates and a total of 11 and 15 individual cell. Mean and standard deviation was plotted in GraphPad Prism. All details of quantification and statistical analyses are also described in the relevant Figure legends and STAR Methods section in detail.